Structure of the plumbing system at Tungurahua volcano, Ecuador: Insights from phase equilibrium experiments on July-August 2006 eruption products

Joan Andújar, Caroline Martel, Michel Pichavant, Pablo Samaniego, Bruno Scaillet, Indira Molina

To cite this version:

Joan Andújar, Caroline Martel, Michel Pichavant, Pablo Samaniego, Bruno Scaillet, et al.. Structure of the plumbing system at Tungurahua volcano, Ecuador: Insights from phase equilibrium experiments on July-August 2006 eruption products. Journal of Petrology, 2017, 58 (7), pp.1249-1278. 10.1093/petrology/egx054 . insu-01583929

HAL Id: insu-01583929

https://insu.hal.science/insu-01583929v1

Submitted on 8 Sep 2017

Structure of the plumbing system at Tungurahua volcano, Ecuador: Insights from phase equilibrium experiments on July-August 2006 eruption products

Joan Andújar[1,*], Caroline Martel[1], Michel Pichavant[1], Pablo Samaniego[2], Bruno Scaillet[1], Indira Molina[3]

1. Institut des Sciences de la Terre d'Orléans, CNRS-Université d'Orléans-BRGM, 1a rue de la Férolerie, 45071, Orléans France
2. Laboratoire Magmas et Volcans, Université Clermont Auvergne, CNRS, IRD, OPGC, F-63000 Clermont-Ferrand, France

3. Instituto Geofísico, Escuela Politécnica Nacional, P.O. Box 17-01-2759, Quito, Ecuador

*Corresponding author: Joan Andújar

phone number: (+33) 2 38 25 54 04

Fax: (+33) 02 38 63 64 88

e-mail address: Juan.Andujar@cnrs-orleans.fr

Caroline Martel e-mail address: Caroline.Martel@cnrs-orleans.fr

Michel Pichavant e-mail address: pichavan@cnrs-orleans.fr

Pablo Samaniego e-mail address: pablo.samaniego@ird.fr

Bruno Scaillet e-mail address: bscaille@cnrs-orleans.fr

Indira Molina e-mail address: indimolina08@gmail.com

ABSTRACT

Understanding the plumbing system structure below volcanoes and the storage conditions (temperature, pressure, volatile content and oxygen fugacity) of erupted magmas is of paramount importance for eruption forecasting and understanding of the factors controlling eruptive dynamics. Phase equilibria experiments have been performed on a Tungurahua andesite (Ecuador) to shed light on the magmatic conditions that lead to the July-August 2006 eruptions and the parameters that controlled the eruptive dynamics. Crystallization experiments were performed on a representative August 2006 mafic andesite product between 950-1025ºC, at 100, 200 and 400 MPa and NNO+1 and +2, and water mole fractions in the fluid (XH_2O) from 0.3 to 1 (water-saturation). Comparison of the natural phenocryst assemblage, proportions and phenocryst compositions with our experimental data indicates that the natural andesite experienced two levels of ponding prior to the eruption. During the first step, the magma was stored at 400 MPa (15-16 km), 1000ºC, and contained ca. 6 wt % dissolved H_2O. In the second step, the magma rose to a confining pressure of 200 MPa (8-10 km), where subsequent cooling (down to 975ºC) and water-degassing of the magma led to the crystallization of reversely zoned rims on pre-existing phenocrysts. The combination of these processes induced oxidation of the system and overpressure of the reservoir, triggering the July 2006 eruption. The injection of a new, hot, volatile-rich andesitic magma from 15-16 km into the 200 MPa reservoir shortly before the eruption, was responsible for the August 2006 explosive event. Our results highlight the complexity of the Tungurahua plumbing system in which different magmatic reservoirs can co-exist and interact in time and are the main controlling factors of the eruptive dynamics.

INTRODUCTION

Volcanic eruptions in populated areas represent a major threat to human beings, having both regional economic and social impacts and global consequences. Nowadays, the monitoring of active volcanoes helps to forecast volcanic eruptions with several days or weeks of anticipation. However, geophysical techniques do not allow prediction of the eruptive style of an incipient or on-going eruption. This task usually involves consideration of the eruptive history of the volcano, which very often records significant variations in eruptive style during a single event, or during the lifetime of a volcano. Regardless of the volume of material extruded, the eruptive activity displayed by a volcanic system falls into two broad categories:

either purely effusive events, typically generating lava flows or domes, or explosive ones that generate Strombolian, Vulcanian or Plinian eruptions with associated pyroclastic flows. The transition between effusive and explosive activity has been the focus of numerous petrological, numerical simulation and experimental studies (e.g., Jaupart & Allègre, 1991; Martel *et al*., 1998; Andújar & Scaillet, 2012b). Proposed causes involve differences in the volatile content of the magma, compositional and volatile stratification of the magma chamber, changes in vent conditions, changes in levels of magma storage or magma compositions, processes occurring during magma ascent to the surface (e.g. magma degassing in the conduit, differences in ascent velocity, variation in the rheological properties of the magma; Sparks *et al*., 1994; Martel & Schmidt, 2003; Martel, 2012; Castro & Mercer, 2004; Scaillet *et al*., 2008; Andújar & Scaillet, 2012b; Andújar *et al*., 2013).

Since large explosive events likely result from the interplay of various processes, their forecasting and understanding still represent a major challenge to the volcanological community. Additionally, the causes leading to either effusive or explosive eruptions may be different for different volcanoes (depending on the geodynamic context, magma composition and gas content, involved magmatic volumes, etc…), so that there is a necessity to address the eruptive dynamics on a specific basis for each volcanic system. From this work we aim to understand the factors that control the eruptive dynamics (i.e. effusive *versus* explosive, long-lasting intermediate explosive *versus* short-lived highly explosive events) at Tungurahua, Ecuador, with emphasis on the role played by dissolved volatiles, magma composition and relative location of the reservoir(s) below the edifice.

TUNGURAHUA VOLCANO: GEOLOGICAL SETTING AND VOLCANIC ACTIVITY

Active volcanoes monitored by a permanent sensor network provide a variety of data that illuminate the on-going magmatic processes occurring below the edifice (e.g., El Hierro in Canary Islands, López *et al*. 2012; Martí *et al*. 2013). However, current geophysical and geochemical techniques still need to be improved in order to discriminate between magma or gas movement within a volcanic edifice, especially when the seismic signals do not have simple decaying oscillations as the one shown by Molina *et al*. (2004) for Tungurahua volcano. In other cases, the density of the geophysical network or the presence of aquifers at near surface levels make it difficult to identify the presence of deep magma reservoirs and, or, conduits. This is the case of Tungurahua volcano (5023 m above sea level - asl), located in the Eastern Cordillera of the Ecuadorian Andes, one of the most active volcanoes in Ecuador, along with other large edifices like Cayambe, Antisana, Cotopaxi and Sangay (Fig.1). During the last millennia, Tungurahua volcano frequently emitted andesitic magmas during medium-to-high explosive eruptions (VEI ≤ 3) that generate tephra fallouts, pyroclastic flows and lahars, together with blocky lava flows (Hall *et al.*, 1999; Le Pennec *et al.*, 2008; 2016). These eruptions display a minimum recurrent time of at least one pyroclastic flow-forming eruption per century and include the historical eruptions of AD 1640, 1773 and 1916-1918. However, the volcano stratigraphic sequence also records the occurrence of much more explosive events (VEI ≥ 4), characterized by regional tephra fallout and pumice pyroclastic flows that involve dacitic magmas (Hall *et al.*, 1999; Le Pennec *et al.*, 2013), the most recent being the large AD 1886 dacitic plinian event (Le Pennec *et al.*, 2016; Samaniego *et al.* 2011).

After 75 years of repose, Tungurahua initiated a new eruptive period in 1999, which is still on-going (March 2017, Fig. 1; IGEPN reports at www.igepn.edu.ec/tungurahua-informes). From 1999 to 2005 the eruptive activity typically consisted of recurrent low-to-moderate explosive phases, characterised by a strombolian style, with short duration (canon-like) explosions that fed small volcanic plumes reaching up to 7 km above the summit, and local ash fallout. In April 2006, a new unrest period started with seismicity moving from deep (15 km) towards very shallow depths (< 5 km) (IGEPN reports) as well as a change in the degassing pattern of the volcano (Arellano *et al.*, 2008), ending with the July-August 2006 paroxysmal phase that generated a ~15 km asl sub-plinian column, a regional tephra fallout and several pyroclastic flows that descended over the flanks of the volcano (Samaniego *et al.*, 2011; Eychenne *et al.*, 2013; Hall *et al.*, 2013).

The eruptive products from the 1999-2005 events have a homogeneous andesitic composition (58-59 wt.% SiO_2). In comparison, samples from the historical eruptions of Tungurahua (AD 1641, 1773, and 1918) display a wider silica content (56-59 wt% SiO_2). In contrast, during the 2006 paroxysmal eruption, two different types of magma were erupted: a very minor dacitic (61-65 wt% SiO_2) component (< 1 vol.%, Eychenne *et al.*, 2013), with characteristics akin to those of the AD 1886 products, dispersed into a homogeneous and volumetrically dominant mafic andesite (58-59 wt% SiO_2).

In this study, we have experimentally investigated the phase relationships of the 2006 andesite from Tungurahua, in order to determine the conditions of magma storage and differentiation (pressure, temperature, volatile fugacities) and shed light on the structure of the plumbing system. Along with these volcanological aspects, Tungurahua and other volcanic edifices of the Northern Volcanic Zone of the Andean arc in Ecuador (i.e., Antisana, Pichincha, Sangay, Cayambe) are known to erupt geochemically distinctive products, characterized by primitive magnesian andesites with Mg#>50 (Kelemen *et al*. 2014) with an adakitic affinity (e.g., Bourdon *et al*. 2002a,b; Garrison & Davidson 2003; Samaniego et al. 2005; Hidalgo *et al*. 2012, among others). Intermediate to silicic adakitic magmas have been previously studied (e.g., Mt. Pinatubo, Scaillet & Evans, 1999; Prouteau & Scaillet, 2003) but mafic compositions with an adakitic affinity such as those erupting at Tungurahua have been left virtually uncharacterized experimentally. Although similar rocks such as high-Mg andesites have been investigated by Blatter & Carmichael (1998), Moore & Carmichael (1998) and Wood & Turner (2009), data on the Tungurahua andesite presented in this study contribute to the experimental database for mafic magmas close to the adakitic series.

Previous Constraints on the Tungurahua plumbing system

Although Tungurahua is a permanently monitored volcano characterized by a high eruption frequency since 1999, to date there is no consensus about magma storage conditions, in terms of depth, temperature, or gas content. Molina *et al*. (2005) obtained a tomographic image of Tungurahua volcano and inferred that the presently active magmatic conduit system probably coincides with vertically aligned earthquake hypocenters that span over 4-5 km below the summit. These are located just above the vertically oriented high-velocity core interpreted as the source zone recharging the shallow magmatic system which is located 5 to 6 km below the summit. Molina *et al*. (2005) suggested that a main magma body is likely to exist beneath this high-velocity zone, although the resolution of tomographic images is poorer at such depths. For instance, hypocenter locations of volcano-tectonic earthquakes are extensively scattered from 6-17 km below the summit, in a large region likely to host a magma body (see *Figure 5d* from Molina *et al*., 2005). Recent data have shown that eruption events recorded in 2010 were triggered 6 km below the summit (Kumagai et al., 2011), which is interpreted as the depth at which magma is subjected to pressure disturbances, further resulting in fragmentation of the magma at shallower depths. In addition, Biggs *et al*. (2010) using synthetic aperture radar interferometry (InSAR) images of Tungurahua during the February 2008 eruption, reported a rapid uplift associated with a shallow sill-like magmatic source inside the Tungurahua cone.

Based on petrological constraints on the July-August 2006 eruptive products, Samaniego *et al.* (2011) estimated pre-eruptive temperatures between 950-1015ºC and pressures of 200-250 MPa (i.e. ~7-10 km below the summit) for the magma reservoir. Myers et al. (2014), based on the study of melt inclusions (MI) trapped in mineral phases (olivine, pyroxene, plagioclase) from basaltic andesite and andesite of the 2006 and 2010 eruptions, reported dissolved H_2O contents up to 4 wt% and pressures of 50-100 MPa for Tungurahua magmas. It should be noted that these are minimum saturation pressures since CO_2 was not measured or was present in very low amounts (< 250 ppm; Myers *et al.*, 2014).

Lastly, the study of InSAR images acquired during the 2003-2009 period at Tungurahua allowed Champenois *et al.* (2014) to identify a large-scale (at least 20 km in diameter) uplift region, located just to the west of the Tungurahua stratovolcano (but including it). These authors suggested that the observed deformation was due to a recharge episode into a magma body located at 11-12 km below sea level (i.e. 15-16 km below the summit of Tungurahua).

Altogether, the above suggest that the Tungurahua magmas are stored over a wide range of depths ranging from 6 to 17 km below the summit (at pressures from 50 to 400 MPa). Thus, our phase equilibrium experiments were aimed at covering the conditions that match these estimations, i.e. pressures between 100 and 400 MPa, temperatures of 950-1025-ºC, water contents from saturated to nominally-dry and oxygen fugacity (fO_2) between NNO+1 and NNO+2.

EXPERIMENTAL SAMPLE

Bulk-rock

We used as starting material the scoriae lapilli products of the August 2006 episode corresponding to sample TUNG-PS-51B of Samaniego *et al.* (2011). Further analytical and petrographic work was performed to complete the available data concerning the petrography and chemistry of the August 2006 products (see below for the analytical conditions). The sample is a Mg-rich mafic andesite (58 wt % SiO_2; Table 1). It exhibits an adakitic affinity

(Defant & Drummond 1990), marked by elevated MgO (4.5 wt %) and Na_2O (3.9 wt %), high Sr (570 ppm) and La/Yb (12) and a low Y (17 ppm; Table 1). TUNG-PS-51B and the other Tungurahua samples plot mid-way between typical Cenozoic adakites and island arc magmas in geochemical discrimination diagrams (Drummond *et al.*, 1996). In a $Mg\#_{gl/whole\text{-}rock}$ (=100*MgO/MgO+FeO*) *vs* SiO_2 diagram, TUNG-PS-51B plots in the same group as other mafic Tungurahua magmas (Fig 1c), demonstrating that our sample is representative of the August 2006 products, as well as of the basaltic-andesite magmas erupted at Tungurahua. The good match between the TUNG-PS-51B bulk-rock and glass inclusion compositions (Fig. 1c) suggests that our starting material represents a "true" liquid characteristic of the Tungurahua magmatic system.

Phase assemblage and compositions.

The mineralogy is dominated by phenocrysts of plagioclase (Pl), clinopyroxene (Cpx), orthopyroxene (Opx), and magnetite (Mt); some crystals of resorbed olivine (Ol) and ilmenite (Ilm) are also present (Table 1, see Supplementary Data Appendix natural sample). This assemblage is set in a highly vesiculated matrix.

Plagioclase.

Pl appears as euhedral to subhedral crystals with sizes up to 1 mm. The main population of Pl has an average composition of $An_{51\pm4}Ab_{46\pm3}Or_{3\pm0.5}$, with slight normal zoning (cores of An_{60} and rims of $An_{51;}$ Fig. 2a). In addition, the presence of reversely zoned plagioclases in the andesite, with cores of An_{51} and rims of $An_{65\text{-}70,}$ is a remarkable feature (i.e., Samaniego *et al.* 2011). We stress that this Ca-rich composition was only found as part of Pl rims and never as single isolated crystals.

Clinopyroxene.

Cpx appears as euhedral to subhedral crystals with sizes similar to those of plagioclase. They have a homogeneous core-to-rim composition of $En_{41\pm1}$ $Fs_{18\pm2}$ $Wo_{41\pm1}$, and a Mg# of 69±1 (Mg#=100* Mg/(Mg+Fe*) in moles; Fig. 2, Table 1). However, 40-50 vol.% of the crystals show a reverse zoning pattern with rim compositions of $En_{46\pm1}Fs_{11\pm1}Wo_{43\pm0.5}$ and Mg# of 81±2 (Fig 2b). These compositional variations encompass those already observed for the same 2006 mafic andesite by Samaniego *et al*. (2011).

Orthopyroxene.

The main Opx population (~500 μm to up to 1 mm) has a composition of $En_{67\pm2.5}Fs_{30\pm1}Wo_3$, and a Mg# of 69±1. However, when compared to Cpx, most crystals do not show any compositional variation over their long axis (Fig. 2b). Only rare Opx crystals have a more Mg-rich composition of $En_{74\pm1}Fs_{23\pm11}Wo_3$, and an Mg# of 76±1 (Fig. 2b). As for Cpx, both Opx populations appear as isolated crystals within the sample. A few of them, however, display complex textural relationships with Cpx. We identified a Cpx crystal ($En_{41}Fs_{18}Wo_{41}$, Mg# = 69) surrounded by an Opx of composition $En_{74}Fs_{22}Wo_3$ and Mg# = 77 (Fig. 2b). Again, Opx compositional zoning matches that which was reported by Samaniego *et al.* (2011) on 2006 mafic andesite products.

Ti-Magnetite.

Mt is quite scarce, appearing as euhedral to subhedral crystals with sizes between 100-200 μm. The main population has a homogeneous composition, with FeO* (total Fe as FeO) = 75±1 wt %, TiO_2 = 11±0.2 wt % and Cr_2O_3 = 0.54±0.2 wt %, being similar to that previously found by Samaniego *et al*. (2011).

Matrix glass

The residual glass has an average composition of silicic andesite, with 63 wt % SiO_2, 16 wt % Al_2O_3, 6 wt % FeO*, 7 wt % Na_2O+K_2O, and 2.3 wt % MgO (Table 1). This glass composition is, within analytical error, the same as found for the same eruption product by Samaniego *et al.* (2011; see Supplementary Data appendix natural sample).

Other mineral phases

Dispersed within the vesiculated matrix, we occasionally found (<0.5 vol.%; Samaniego *et al*., 2011) Ol phenocrysts, normally zoned from $Fo_{80\pm2}$ cores to $Fo_{75\pm2}$ rims (Samaniego *et al*., 2011; Myers *et al*., 2014). These crystals show clear evidence of reaction, i.e. they have resorbed rims overgrown by an Opx of composition $En_{71}Fs_{25}Wo_4$ and Mg# = 75

(Supplementary Data Appendix natural sample). The origin of such textural relationships and compositional zoning of Ol and related Opx is addressed subsequently.

We also found a partially resorbed Ilm crystal (41 wt % TiO_2, 49 wt % FeO*) surrounded by a Mt crystal with a composition similar to that of the main population (TiO_2 = 13 wt%, Mg# = 5). Taking into account the Ilm-Mt equilibrium test of Bacon & Hirschmann (1988) and using the model of Sauerzapf *et al*. (2008), this pair yields a T of 1001ºC and a fO_2 of NNO+0.92 (Supplementary Data Appendix natural sample).

Phase proportions.

Petrographic information, along with mineral and glass compositions, was used to estimate the phase (crystals and glass) proportions in the andesite magma by mass-balance. The andesite contains 56 wt % glass and 44 wt % phenocrysts including 28 wt % Pl (An_{51}), 7.5 wt % Opx (En_{67}), 7.1 wt % Cpx (En_{41}) and 1.1 wt % Mt, (Table 1). If the Ca-rich (An_{65-70}) Pl and the Mg-rich Cpx (En_{46}) and Opx (En_{74}) are used instead of the main compositions, the calculated crystal content decreases to 32 wt % (20 wt % Pl, 6 wt % Opx, 5 wt % Cpx and 1.5 wt % Mt).

EXPERIMENTAL APPROACH AND ANALYTICAL TECHNIQUES

Starting material

The starting glass material for our experimental study was prepared by crushing and milling several pieces of andesitic sample (about 10 g) followed by a two-step fusion of the resulting powder at 1400ºC (with grinding in between) in a Pt crucible at atmospheric pressure for three hours. The composition and homogeneity of the dry glass was verified by electron microprobe (EPMA) and found to be similar to the X-ray fluorescence (XRF) analysis (Table 1; Samaniego *et al*., 2011). The glass was finally ground and stored at 120ºC in an oven to avoid atmospheric hydration.

Capsules

All experiments were run in 1.5 cm long, 2.5 mm inner diameter, 0.2 mm walled Au capsules to minimize Fe loss under reduced conditions. Capsules were prepared following standard procedures (e.g. Scaillet *et al.*, 1995; Martel *et al.*, 1998; Andújar & Scaillet, 2012a) where H_2O is added first, followed by silver oxalate as a source of CO_2 in H_2O-undersaturated charges and finally 30 mg of starting glass powder. The fluid/silicate ratio in the capsules was maintained constant (~10 wt %) to ensure fluid-saturated conditions, which were always achieved by adding 3±0.5 mg of fluid (H_2O+CO_2) to the 30 mg glass powder. For each run, different XH_2O_{in} [=initial $H_2O/(H_2O+CO_2)$ in moles] were explored by adding different proportions of starting H_2O-CO_2 mixtures to the capsule in order to cover an XH_2O_{in} range of 1-0.3, hence different melt water content (H_2O_{melt}) in the experimental glasses (Table 2). Capsules were then arc-welded and inserted in an oil bath to check for possible leaks. Successful capsules were left in an oven at 100ºC for a few hours to allow H_2O to homogenise within the charge before the experiments. We checked systematically the weight of all charges prior to and after the experiments. Capsules were considered successful when the weight difference between each step agreed to within 0.0004 g (which is about the precision of the analytical balance), confirming that no volatiles escaped during the experiments.

Experimental equipment

A total of 62 crystallization experiments were conducted in a vertical Internally Heated Pressure Vessel (IHPV), using Ar as pressurizing medium, which was mixed with different amounts of H_2 at room temperature to achieve the desired fO_2 conditions. We used a double-winding high-temperature molybdenum furnace, which ensures near-isothermal conditions (gradient <2-3ºC) along a 3 cm long hotspot. Temperature and pressure were continuously recorded with two S-type thermocouples and a pressure transducer, with an accuracy of ±5ºC and ±20 bars, respectively. A typical run contained 4 to 5 capsules loaded with silicate+fluid components plus an extra capsule containing a Ni-Pd-O redox sensor (see Taylor *et al.*, 1992) to monitor the prevailing fH_2 at the desired T-P. Each set of charges was run at the selected T-P-fH_2 for an average of about 90 hours and terminated by a drop quenching (Table 2; Andújar & Scaillet, 2012a; Di Carlo *et al.*, 2006). At the end of all experiments, we systematically observed a rise of the total pressure indicating that the sample holder had fallen into the bottom cold part of the vessel and that drop quench was successful (quench rate >100°C/s). After the experiments capsules were checked for leaks by weight comparison (see above), opened, and some pieces of the run products were embedded in epoxy and polished for optical observation and subsequent Scanning Electron Microscope (SEM) and electron microprobe (EMP) analyses.

Analytical techniques

The natural rock, starting glass and experimental run products were analysed using a SX-FIVE electron microprobe at ISTO-BRGM in Orléans (France) using an acceleration voltage of 15 kV, sample current of 6 nA, and 10 s as counting time. Calibration was performed by using the following standards: Si+Na in albite, Ti+Mn in $MnTiO_3$, Al in Al_2O_3, Fe* in Fe_2O_3, Mg in MgO, Ca in andradite, K in orthoclase, Cr in Cr_2O_3, Ni in NiO and P in apatite. A focused beam was employed for analysing minerals (both natural and experimental), whereas a defocussed 10μm beam was used for experimental glasses to minimize alkali migration (i.e., Devine *et al.*, 1995; Andújar & Scaillet, 2012a). In addition, crystal-free or near-liquidus charges (i.e., T10, T28) were analysed first in each probe session to assess the correction due to alkali migration for the determination of H_2O_{melt} in crystal-bearing charges with the "by-difference" method (Devine *et al.*, 1995).

We calculated phase proportions (wt %) by performing mass-balance calculations with the XLFRAC programme (Stormer & Nichols, 1978) for charges where we could successfully analyse the composition of the mineral and glass phases. However, in charges having small crystal sizes (<5 μm), it was difficult to obtain electron microprobe analyses without glass contamination, in particular for Mt and Pl. In this case, we used the compositions of minerals from other charges run at the same P-T-fH_2 conditions (Table 2). Glass composition is normalized to a 100 wt % anhydrous basis to avoid any compositional effect due to the dissolved H_2O_{melt}. Calculated phase proportions (wt %), and the corresponding sums of residuals (ΣR^2, usually ≤ 0.5) are given in Table 2.

Water content, fH_2, fO_2 in the experimental charges

The different H_2O+CO_2 mixtures (thus the different XH_2O_{in}, Table 2) in the capsules allowed us to explore different melt water contents (H_2O_{melt}), which were determined as follows. In runs containing low-to-medium crystal contents, the H_2O dissolved in glass was obtained from the difference between the glass analyses and 100 wt % (*cf.* Devine *et al.*, 1995), as determined by using near-liquidus charges (i.e., typically T10 and T28) as standards. In charges characterised by a high crystal content (>25-30 wt %; Table 2) and an homogeneous distribution of the mineral phases (see below), EMP analysis of the residual glass was difficult and so, the "by-difference" method could not be applied. Thus, for internal consistency and to restrict the use of different methodologies, the water content dissolved in all charges was determined by using the method of Scaillet & Macdonald (2006). This was achieved first by calculating H_2O_{melt} for each experimental charge under water-saturated conditions and for any given P-T by using the water solubility model of Papale *et al.* (2006). Second, these data were used along with f^oH_2O (the fugacity of pure water at the relevant P-T, Burnham *et al.* 1969) to calibrate an equation of the form f^oH_2O (in bars)=a(H_2O_{melt} (wt %)$)^b$, in which the retrieved coefficients were a = 51.19 and b = 2.06 (R^2=0.991). Third, for each water-undersaturated charge, we used the relationship $fH_2O=f^oH_2O \times XH_2O_{in}$ to calculate the fH_2O for each charge, and the respective H_2O_{melt} was retrieved by inverting the above equation: H_2O_{melt}(wt %)=(fH_2O/51.19$)^{1/2.06}$. With H_2O_{melt} calculated using this methodology, the main source of uncertainty concerns the determination of fH_2O and the assumption that $XH_2O = XH_2O_{in}$ (see Scaillet & Macdonald, 2006). To assess the impact of these parameters on calculated H_2O_{melt}, we systematically varied fH_2O and XH_2O and found that changes of 100 to 300 bars on fH_2O or ±0.15 in XH_2O_{in} produce a variation on $H_2O_{melt} \leq 0.7$ wt %.

We stress that the above procedure is equivalent to assuming ideal behaviour in the H_2O-CO_2 fluid phase, and neglects the amount of H_2O lost by the fluid through dissolution into the melt: hence, retrieved values must be considered as maximum melt water contents (e.g., Berndt *et al.*, 2005; Scaillet & Macdonald, 2006; Andújar *et al.*, 2015). However, the water contents calculated following this procedure and those obtained with the standard "by-difference" method were found to agree within relative analytical errors (±1.3 wt %; Table 2).

As mentioned before, we used Ni-Pd-O sensors to determine the prevailing fH_2 and, ultimately, the fO_2 specific to each charge (see below). Two contrasted redox conditions were explored: (1) NNO+0.79 (±0.31 log units, here after referred to as NNO+1 experiments) and (2) NNO+1.90 (±0.19 log units see Table 2, here after referred to as NNO+2 experiments); these values corresponding to the water-saturated charges. However, for each P-T-fH_2, the fO_2 decreases with decreasing aH_2O (or XH_2O_{in}; see Scaillet *et al.*, 1995; Freise *et al.*, 2009; Andújar & Scaillet, 2012a). Thus, the water-undersaturated charges have a fO_2 lower than the values above (see Scaillet *et al.* 1995; Berndt *et al.* 2005; Andújar & Scaillet 2012a). In detail, calculated fO_2 for charges from the NNO+1 experiments ranged from NNO+1.22 to NNO-

0.85 whereas, for the NNO+2 experiments, the fO_2 varied from NNO+0.94 to NNO+2.2 (Table 2; for more details see Andújar & Scaillet, 2012a; Andújar *et al.*, 2015).

Overall, the crystallization experiments successfully covered the range of conditions inferred so far for the Tungurahua magmatic system: temperature: 950-1025ºC; pressure: 100-400 MPa; fO_2 : NNO+1 - NNO+2 (Table 2).

Attainment of equilibrium

The experimental procedure followed in this work is similar to that of previous studies where near-equilibrium conditions were achieved (e.g., Martel *et al.*, 1999; Costa *et al.*, 2004; Berndt *et al.*, 2005; Andújar *et al.*, 2015). Different observations from our run products show that near-equilibrium conditions were also attained in this study: the euhedral shape of crystals, the homogeneous distribution of phases within the charges, the smooth variation of phase proportions and compositions with changes in experimental conditions, the fact that calculated crystal-liquid exchange coefficients (Kd) for olivine, clinopyroxene and plagioclase are similar to those from the literature when calculated under similar conditions (see below), and the small sum of residuals (generally ≤ 0.5; Table 2) of mass-balance calculations, the latter indicating that no major phase has been omitted. Experimental run durations (≤ 115 hours) are within the range of other studies performed on andesitic compositions for which near-equilibrium conditions have been also claimed (e.g. Moore & Carmichael, 1998; Almeev *et al.*, 2013).

RESULTS

Mineral phases identified in run products include Ol, Cpx, Opx, Pl, Amph (amphibole), Mt, and Ilm. For each charge, the phase assemblage and calculated proportions are given in Table 2. The relationships between the different mineral phases and the effect of T, P, H_2O_{melt} content and fO_2 on their stability are displayed in a series of isobaric-polythermal or isothermal-polybaric diagrams (Figs. 3a to f). The position of the different mineral saturation curves was first defined from the identified phase assemblages and then refined by using the phase proportions from Table 2.

Phase relationships at fO_2~NNO+1

At 200 MPa, Ol, Mt and Cpx are the liquidus phases and dominate the hottest and water-rich part of the diagram (960-1020ºC; 5-6 wt % H_2O; Fig. 3a). A decrease in H_2O_{melt} and temperature results in the crystallization of Pl+Opx, followed by Ilm until temperatures slightly below 980ºC and $H_2O_{melt} < 3$ wt % are reached. Amph is stable only below 960ºC and at water-rich conditions (5-6 wt % H_2O_{melt}), being replaced by Opx at lower H_2O_{melt} (Fig. 3a). Olivine is not stable below 980ºC and 5 wt % H_2O_{melt}, and the assemblage Opx+Pl+Cpx+Mt+Ilm is stable in the dry part of the diagram. A decrease in pressure from 200 to 100 MPa enhances the Pl stability field, where Pl co-crystallizes with Ol+Cpx at near-liquidus conditions (Fig. 3b), and the Mt-in curve is depressed by ~25ºC. Ol stability also extends to a lower temperature than at 200 MPa. At 1000ºC, Ol, Cpx and Pl are joined by Opx and Ilm when H_2O_{melt} is decreased. Increasing pressure from 200 to 400 MPa has an important effect on the phase relationships. Liquidus conditions are achieved at 1025ºC and ~9 wt % H_2O_{melt}. At this temperature, the sequence of crystallization upon decreasing H_2O is: Cpx, Opx, Mt and then Pl, this last phase appearing later in the sequence than at 200 MPa. Ol is not part of the liquidus phase assemblage at 400 MPa. It has a restricted stability field, appearing at ≤1010ºC and for H_2O_{melt} contents between 9 and 7.5 wt % (Fig 3c). Ilm appears at the same temperature as Ol, but at $H_2O_{melt} \leq 5$ wt % (Fig 3c).

Phase relationships at fO_2~NNO+2

Increasing fO_2 to NNO+2 affects mineral stabilities to various extents depending on the prevailing pressure. At 100 and 200 MPa, such an increase in fO_2 suppresses Ilm crystallization, and strongly shifts the Ol stability field towards the water-rich part of the diagram ($H_2O_{melt} >$ 4-6 wt %; Fig. 3a, b). As a result, at lower H_2O_{melt} contents, the dominant phase assemblage is Opx+Cpx+Pl+Mt (Fig. 3a). At 400 MPa, Ol is conspicuously absent in charges run at NNO+2 (Fig. 3d). Mt becomes the liquidus phase at 1025ºC and 9 wt % H_2O_{melt}, and is followed by Opx+Pl at lower H_2O_{melt} (Fig. 3d). Amph crystallizes at 1000ºC and ~9 wt % H_2O_{melt}, and its stability domain at 950°C expands toward lower H_2O_{melt} (up to 6 wt %) in comparison with at NNO+1). It is worth noting that Cpx is not stable below 960ºC, being replaced either by Opx (+Pl+Mt) or by Amph (+Pl) depending on H_2O_{melt} (Fig. 3d), with a possible peritectic relationship between Amph and Cpx (e.g., Rutherford, 2008).

Crystal content and phase proportions

Liquidus conditions (i.e., 0 wt.% crystals) have been attained at 1025ºC, 400 MPa, ~9 wt % H_2O_{melt} and fO_2~NNO+1 (Supplementary Data Appendix crystal content, Table 2) whereas the maximum amount of crystals (45 wt %) occurs at 1025ºC, 400 MPa, 6.6 wt % H_2O_{melt} and fO_2~NNO+1. In general, the crystal content of the charges varies with the experimental parameters, mostly T, H_2O_{melt} and P, whereas a change in fO_2 from NNO+1 to NNO+2 does not have a major influence (see Supplementary Data Appendix crystal content). Lowering H_2O_{melt} and temperature at a given pressure increases the crystal content (see for instance the 200 and 400 MPa charges; Table 2). For charges with the same range of H_2O_{melt} (4-6 wt %) at the same temperature (i.e., 1000ºC), the crystal content is positively correlated with pressure (appendix crystals; Table 2). Mt and Ol are present in low amounts, never exceeding 4 wt %. At the onset of crystallization, Opx is present in low amounts (< 1 wt %), its proportion progressively increasing (up to 9 wt %) with decreasing H_2O_{melt}. The amount of Cpx increases rapidly with decreasing H_2O_{melt} and temperature, achieving a maximum of 13 wt % (see charge T36 in Table 2); however, the increase is not as high as that for plagioclase, which rapidly becomes the dominant mineral phase when present (Table 2).

Phase compositions

Experimental phase compositions (minerals and glass) are displayed in Tables 3 to 9 and their variation with experimental variables (P-T-fO_2 and H_2O_{melt}) is discussed in the following sections.

Olivine

Experimental Ol ranges in composition from Fo_{64} to Fo_{81}. The maximum Fo content was reached at 1000ºC, 200 MPa and fO_2~NNO+2, whereas the lowest Fo was obtained at 950ºC, 200 MPa, fO_2~NNO+1, both charges, however, containing similar H_2O_{melt} (~6 wt %, Table 3). At a given pressure and temperature, a decrease in H_2O_{melt} decreases drastically the Fo content of Ol; this is exemplified by the series at 200 MPa and NNO+1 in which a decrease of ~2 wt % in H_2O_{melt} decreases the Fo content of Ol by about ~13 mol% (Fig 4a). A decrease in temperature also affects Ol composition at a given H_2O_{melt} and pressure. At higher temperatures (1000ºC-975ºC) and H_2O_{melt}, the effect of T is maximum: a decrease of 25ºC reduces by 5 mol% the Fo content. In lower temperature (thus more crystallized) charges, the influence of temperature becomes less important (Table 3, Fig 4a; Andújar *et al.*, 2015; Berndt *et al.*, 2005; Di Carlo *et al.*, 2006).

In our work, the effect of changing fO_2 remains modest since the difference between the two differents series is generally ~1.5 log unit (Table 2). Notwithstanding, this fO_2 variation produced changes in Ol composition of 2-4 mol% Fo at a given pressure, temperature and H_2O_{melt} (i.e., see charges T10 and T45b at 1000ºC/200 MPa and 6 wt % H_2O_{melt}).

At any given temperature, fO_2 and pressure, the CaO content in Ol increases with decreasing H_2O_{melt}, Fo content, and increasing crystal content (hence with SiO_2 enrichment, see below), in agreement with previous experimental studies (Fig. 4b; Libourel, 1999; Berndt *et al*., 2005; Di Carlo *et al*., 2006; Feig *et al*., 2006; Andújar *et al*., 2015).

The average olivine-liquid exchange (Kd^{Fe*-Mg} ; using FeO* as total iron) is 0.27 (varying between 0.22 to 0.31); whereas when Kd^{Fe*-Mg} is calculated with melt Fe^{2+}/Fe^{3+} estimated by the method of Kress & Carmichael (1991), the exchange coefficient varies between 0.34-0.45 (Table 3). These values are in good agreement with previous experimental studies (Sisson & Grove, 1993; Pichavant *et al*., 2002; Barclay & Carmichael, 2004; Feig *et al*. 2006), confirming that our calculated fO_2 values are correct and that equilibrium was likely attained in our experimental runs.

Clinopyroxene

According to the classification of Morimoto (1989) our experimental Cpx are diopsides and augites with compositions in the range En_{41-48} Fs_{10-29} Wo_{23-44}, Mg# = 62-83, TiO_2 = 0.3-1 wt % and Al_2O_3 = 2-5 wt % (Table 4; Fig 5).

The main parameter affecting the Cpx composition is H_2O_{melt} since a variation of 5 wt % produces a change of 10 mol% Mg#; for example, in series conducted at 400 MPa (charges T33 to T36, Table 2) the Cpx changes from $En_{46}Fs_{10}Wo_{43}$, Mg# = 82 to $En_{42}Fs_{18}Wo_{40}$, Mg# = 70 when H_2O_{melt} is reduced from 9 to 7 wt %.

As stated previously, a decrease in H_2O_{melt} increases the crystal content of the charges and the residual melt evolves towards more silicic compositions (Table 2; Supplementary Data Appendix crystals, see below). Thus, apart from H_2O_{melt} variations, the Cpx is also sensitive to the degree of evolution of the liquid. A progressive enrichment in the SiO_2 content of the residual melt produces Cpx that are richer in En, Fs and TiO_2 and poorer in

Al_2O_3, Mg#, and Wo (Fig. 5), as observed in previous studies (Pichavant & Macdonald, 2007; Andújar *et al.*, 2015). As for olivine, the modest increase in fO_2 has little effect on Cpx composition (Fig 5, Table 4) and crystals from charges run at NNO+1 and NNO+2 partially overlap. However, compared to Ol, the effect of pressure on Cpx composition is more marked; a decrease in pressure produces En- and Wo-richer and Fs-poorer Cpx, in particular at pressures < 200 MPa and H_2O_{melt} < 5 wt % (Fig. 5). In contrast, changes in temperature have small effects on Cpx (< 5 mol% of En, Fs and Wo) when compared to those resulting from H_2O_{melt} and pressure variations (see above). Calculated $Kd^{Fe^*\text{-}Mg}$ of clinopyroxene-liquid pairs (calculations performed using FeO*in both melt and Cpx) vary between 0.17 to 0.32, with an average value of 0.24, again in agreement with previous results (Table 4; Berndt *et al.*, 2005; Di Carlo *et al.*, 2006; Andújar *et al.*, 2015)

Orthopyroxene

Representative analyses of experimental Opx are reported in Table 5. Since the Mg# of co-existing Opx and Cpx correlate with each other, within 1-4 mol%, in charges run at the same T, P, H_2O, fO_2 (Tables 4, 5), we expect that the variation of intensive parameters generates compositional changes in Opx that are similar to those in Cpx. The Mg-richest Opx has a composition $En_{77}Fs_{19}Wo_4$, Mg# = 80 at 1025ºC, 400 MPa, NNO+1 and for 8 wt % H_2O_{melt}, whereas the Mg-poorest ($En_{62}Fs_{33}Wo_4$, Mg# = 65) crystallised at the same fO_2 but at somewhat lower T (975ºC), P (200 MPa) and H_2O_{melt} (4 wt %); all experimental Opx compositions lie in between these two end-members (Fig. 6, Table 5). In a similar way as for Cpx, a decrease in H_2O_{melt} of 1 wt % (at a given T and P) increases En- and Mg# and decreases Fs by 10 mol% (i.e., see charges T2 toT4 at 975ºC, 200 MPa), while Wo remains unaffected. A similar compositional change is produced by a temperature decrease of about 75ºC (i.e., charges T51, T39, T44 at 400 MPa, NNO+2). In comparison, an fO_2 increase from NNO+1 to NNO+2 has a smaller compositional effect on Opx (≤ 5 mol% on En), being more marked at 100 MPa than at 200-400 MPa. In those charges where Opx and the coexisting melt compositions were available, the calculated $Kd^{Fe^*\text{-}Mg}$ exchange coefficient between crystal and liquid (again, FeO* in both melt and Cpx were used for the calculations) yielded an average value 0.23 (0.18-0.28; Table 5).

Plagioclase

Changes of Pl composition as a function of H_2O_{melt} are shown in Fig. 7. Experimental Pl compositions are in the range $An_{42\text{-}69}Ab_{31\text{-}53}Or_{0.8\text{-}6}$, the most calcic composition crystallizing at

1000ºC, 100 MPa, NNO+1 and 4 wt % H_2O_{melt} and the least calcic at 950ºC, 400 MPa, NNO+2 and 6 wt % H_2O_{melt} (Fig. 7, Table 6). As already observed in previous experimental studies performed on hydrous basaltic andesite melts, Pl composition is highly sensitive to changes in H_2O_{melt} (Sisson & Grove, 1993; Pichavant *et al.*, 2002). This behaviour is well illustrated by the runs at 100 MPa in which the An content decreases by almost 15 mol% (and reciprocally Or increases) when H_2O_{melt} decreases by 1 wt % (Fig. 7). Compared to water, changing pressure and temperature produces less marked compositional variations ($\leq$ 5 mol% An), whereas a change in fO_2 has no significant effect (Fig. 7, Table 6). The calculated Pl-liquid Ca-Na exchange Kd in our experimental charges varies between 0.94 to 1.95, having an average value of 1.5, again in agreement with values found for similar basaltic andesite compositions (Table 6; e.g., Sisson & Grove, 1993; Pichavant *et al.*, 2002).

Fe-Ti Oxides

Modal abundances of Fe-Ti oxides are rather low in our experimental charges, never exceeding 3 wt % at NNO+2 and 1.5 wt % at NNO+1 (Table 2). In addition, in most charges, Fe-Ti oxides are of small size ($\leq$ 5 µm), and this prevented us from obtaining reliable analyses, particularly for Ilm whose occurrence was mainly detected by SEM (Table 7). Thus, below we only address the effect of experimental parameters on Mt composition.

As for other Fe-Mg phases, variations in H_2O_{melt} affect the Mg# of Mt: a decrease in H_2O_{melt} decreases Mg# and increases the TiO_2 content (Fig. 8). An increase in fO_2 (NNO+1 to NNO+2) at a given P and T slightly increases Mg# (< 1%), whereas the TiO_2 content is decreased by *ca.* 50 % (Fig. 8). Magnetites crystallised at NNO+1 have distinctly higher TiO_2 contents compared to those at NNO+2 (Fig. 8). The effect of P can only be assessed in charges conducted at NNO+2 and 200-400 MPa, due to the small number of charges in which Mt could be analysed at NNO+1. Results show that a decrease in pressure produces Mt with lower TiO_2 and higher Mg# (Fig. 8, Table 7).

Amphiboles

Experimental Amph is a Ti- or Fe-tschermakitic hornblende according to the classification of Leake *et al.* (1997). The limited amount of data available on Amph prevents us from discussing in detail the compositional dependence of amphibole with intensive parameters. Nevertheless, for a given experimental series at constant T and P, a decrease in H_2O_{melt}

produces amphiboles with lower Mg# and slightly higher Ti (Table 8). Traditionally, changes in Al^{IV} and Al^{VI} in Amph have been related to changes in pressure and temperature, respectively, and used as thermobarometers (i.e., Ridolfi & Renzulli, 2012). Whereas pressures calculated on our experimental 400 MPa amphiboles following Ridolfi & Renzulli (2012) are in relatively good agreement with experimental values (387 to 481 MPa), pressures calculated for the 200 MPa amphiboles overestimate experimental values by ~200 MPa (386-396 MPa). Calculated temperatures also overestimate experimental values by 50 to 100°C (Table 8). As pointed out by Erdmann *et al*. (2014), this likely reflects the influence of melt composition, which is not considered in the formulation of Ridolfi & Renzulli (2012). In particular, the model of Ridolfi & Renzulli (2012) has not been calibrated with andesitic melts as rich in Mg as those of Tungurahua or with andesite compositions such as found at Santorini (i.e., Andújar *et al*., 2015).

Residual glasses

Based on the classification of Le Bas & Streckeisen (1991), our experimental glasses have andesitic to rhyolitic compositions (59-70 wt % SiO_2), some straddling the boundary between the trachyandesite and trachydacite fields (Table 9). The compositional evolution of the residual glasses is mostly controlled by variations in T and H_2O_{melt} (or by the degree of crystallization) and, to a lesser extent, by P and fO_2. Between 1025 and 975ºC, at a fixed P and fO_2, glasses become enriched in SiO_2, TiO_2, Na_2O, K_2O and depleted in MgO, CaO and FeO* (Fig 9). The Al_2O_3 content also decreases with H_2O_{melt}, in particular at or below 200 MPa, where a decrease of H_2O_{melt} by 1 wt % decreases by 3 wt % the Al_2O_3 content of the residual liquid (see charges T54 to T57 at 100 MPa). At higher P (400 MPa) and at an fO_2 of NNO+2, a decrease of either 75ºC or 4 wt % in H_2O_{melt} is required to produce Al_2O_3 variations of the same magnitude in the residual glass. Ti and Fe* display a different behaviour depending on the prevailing fO_2 and temperature. Decreasing the H_2O_{melt} at NNO+1 produces a slight increase in TiO_2 and a decrease in FeO*; runs at NNO+2, 400 MPa and 1025-1000ºC show broadly the same behaviour. However, at NNO+2, a decrease in T down to 950ºC drastically reduces (by 50%) the Ti and Fe* contents of the glass, leading to a strong depletion of the liquid in these elements (Fig. 9).

In addition to the influence of fO_2, there are differences in melt evolution with temperature that can be related to changes in mineral assemblages and phase proportions. The progressive melt evolution between 975-1025ºC reflects the crystallization of the

Pl+Cpx+Opx±Mt-Ilm-Ol mineral assemblage in this temperature interval. Upon lowering temperature, the amount of fractionating Cpx continuously increases, being joined by Opx and coupled with crystallization of a low proportion (< 2 wt %) of Fe-Ti oxides. This results in a progressive enrichment in SiO_2, TiO_2 and Na_2O+K_2O in the melt and a depletion in CaO, MgO and FeO*, Al_2O_3 being little affected. The onset of Pl appearance, and its crystallization as the dominant fractionating phase, accelerates the evolution of the melt, reduces the Al_2O_3 and further increases the alkali content (Fig 9). At 400 MPa and NNO+2, Amph crystallization (in proportions that exceed 12-15 wt % and are up to 25 wt % at 950ºC), combined with Pl in similar amounts, is responsible for a sudden SiO_2 increase in the melt (+10 wt % compared to charges at 1025ºC and 7 wt % H_2O melt).

DISCUSSION

Pre-eruptive conditions of the 2006 andesitic products at Tungurahua

To understand the storage conditions of the 2006 andesite and the magmatic processes occurring prior to the eruption, we compare our experimental data with information previously gained from the natural rock. The comparison of experimental and natural mineral assemblages, compositions, and modal proportions provides tight constraints on the pre-eruptive conditions (T, P, H_2O_{melt}, fO_2) of the Tungurahua magma prior to the 2006 eruption.

We first use the information gained from the main unzoned population of phenocrysts (Cpx+Opx+Mt+Pl) and the core composition of the zoned crystals (Cpx, Pl, Opx) to infer the crystallization conditions of these minerals. Second, we constrain the origin of the Mg-rich (Cpx, Opx) and Ca-rich (Pl) phenocryst rims. Rims and cores correspond to two different crystallization environments that are also separated in time. Unzoned minerals and crystal cores formed early during a first episode. These were later subjected to a second crystallization episode, leading to cores being resorbed with subsequent overgrowth of Mg-rich and Ca-rich rims. Below, we use the experimental results to constrain these two successive crystallization stages.

Early crystallization stage: main population of phenocrysts and crystal cores

The natural andesite is dominated by the mineral assemblage Pl+Cpx+Opx+Mt. From our experimental results, this phase assemblage is stable from 975 to 1025ºC at > 200 MPa (for NNO+1) or, in the same temperature range, at 100 MPa (for NNO+2). The lack of Amph in the mafic andesitic products of the 2006 eruption sets a robust low temperature constraint for the crystallization of the main phenocryst assemblage. For an fO_2 of NNO+1, this minimum temperature can be placed at about 960-970°C (Fig. 3a; c), increasing to higher values (up to 1000-1010ºC) if magmatic conditions are more oxidizing than NNO+1 (Fig. 3d). However, since the phase assemblage Pl+Cpx+Opx+Mt is encountered over a relatively wide range of experimental T, P, fO_2 and H_2O_{melt}, additional constraints such as the compositions of mineral phases are used below to refine the pre-eruptive conditions of phenocryst crystallization.

The En content of natural Cpx (En_{40-42}) is closely reproduced at 400 MPa, 1000ºC with 6-8 wt % H_2O_{melt} (Fig. 5b). Only the 400 MPa data reproduce the natural Cpx compositional range. Besides En, the other natural Cpx compositional parameters (Fs, Wo, Mg#) are also reproduced at these conditions (see Tables 2, 4; Fig. 5). Among the 400 MPa charges, two at NNO+1 (T35-36) and two at NNO+2 (T39-T40) contain Opx, Pl and glass with compositions that all approach their natural counterparts. The natural Opx composition (En_{68}) is best matched by the 1000ºC, 400 MPa, 6 wt.% H_2O_{melt}, fO_2~NNO+0.13 charge (T36; Tables 2, 4, 5), as are the Ca-poor Pl (An_{49-50}; Fig. 7) and the andesitic residual glass (Fig. 9). Although we do not have the Mt composition in T36, the compositional trend defined by charges run at lower pressures (100-200 MPa) for the same oxygen fugacity (NNO+1) rules out an fO_2 as high as NNO+2, since Mt would have a too low TiO_2 compared to the natural composition (Fig 8c). This supports a temperature of 1000ºC and an fO_2 of ~NNO for the early crystallization stage of the andesitic magma.

It should be noted that, for such conditions (1000ºC, 400 MPa, 6 wt % H_2O_{melt}, NNO), the assemblage Cpx+Pl+Opx+Mt should coexist with small amounts of ilmenite (Fig. 3c). However, this mineral was only found in the rock as a resorbed crystal surrounded by Mt. This observation suggests that Ilm was indeed part of the early mineral assemblage but that the conditions of the system later became more oxidizing (see below).

As stated above, the assemblage Pl+Cpx+Opx+Mt is also stable at shallower conditions ($P \leq 200$ MPa; Fig. 3 a, b). However, such low pre-eruptive crystallization pressures can be ruled out since, at these pressures, Cpx and Pl are respectively Mg- ($En \geq 43$, Fig 5) and Ca- ($An \geq 57$, Fig 7) rich, outside the natural ranges. The difficulty of crystallizing

Ca-rich Pl in equilibrium with Mg-rich Cpx at 400 MPa can be explained by: (1) the relatively low Ca/Na of our starting material (Table 1, see above) and (2) the fact that Pl is late in the crystallization sequence at this pressure (Fig 3c). Thus, Pl crystallizes from melts depleted in Ca because of Cpx crystallization, which limits An enrichment (Table 9). In contrast, when Pl crystallizes near the liquidus and at low pressures (P ≤ 200 MPa), the residual melt has enough Ca to precipitate high An Pl.

Late crystallization stage: Ca-rich plagioclase and Mg-rich pyroxene rims

Textural and compositional observations indicate that the Ca-rich Pl and the Mg-rich pyroxene rims crystallized simultaneously in the andesitic magma. Our experimental data can be used again to shed light about their crystallization conditions.

Pl has a large stability field under our explored experimental conditions. Nevertheless, An-rich compositions (≥ 65 mol%, typical of Pl rims) were produced in only 3 charges: T15 (1000ºC, 100 MPa, 4 wt % H_2O_{melt}, NNO+1), T54 (1000ºC, 100 MPa, 4 wt % H_2O_{melt}, NNO+2) and T24 (975ºC, 200 MPa, ~5 wt % H_2O_{melt}, NNO+1.7, Fig. 7). In comparison, at 400 MPa, the An content of Pl is ≤ 60 (Fig. 7, Table 6) which implies that a pressure of 400 MPa is too high for crystallization of the Ca-rich rims.

For charges that reproduce the Ca-rich Pl compositions, the lack of Opx in the two charges T15 and T54 indicates that 100 MPa is too low a pressure. Indeed, the mineral assemblage at 100 MPa, 1000°C, 4 wt % H_2O_{melt} (Ol+Cpx+Pl±Mt) does not reproduce the phenocryst assemblage (Fig. 3b, Table 2), the latter being only found in charge T24. Mt in this charge has a composition (Mg#=5.4 and TiO_2 = 8 wt %), Opx is $En_{75}Fs_{21}Wo_4$, Mg# = 79, Cpx $En_{46}Fs_{13}Wo_{40}$, Mg# = 78, these being in the range of the Mg-rich Cpx-Opx population (rims and isolated crystals) of the natural mafic andesite (Tables 4 to 7). In addition, glass in charge T24 also matches (within analytical errors) the glass composition reported by Samaniego *et al*. (2011) and in this work for the August 2006 eruption products (see Supplementary Data Appendix natural and Table 1). Therefore, the data consistently point to a shallow origin for crystallizing the mafic rim compositions.

However, it is worth noting that under the conditions of charge T24, a small proportion (<0.2 wt %) of Ol (Fo_{77}) is present together with the Mg- and Ca-rich mineral assemblage (Table 2; Fig. 3b). It is emphasized that Fo_{77} is in the range of compositions of olivine rims ($Fo_{75\pm2}$; Fig. 4) which are commonly resorbed. Thus, there is a need to clarify the origin of olivine and the mechanism of olivine resorption in the plumbing system (see below).

Tungurahua's plumbing system

Comparison between our experimental data and the natural andesite allows us to constrain the storage conditions of the magma prior to the eruption. According to our results, the two texturally and chemically distinctive mineral populations crystallized at two different levels. The low-Ca Pl ($An_{50\pm5}$), Mg-poor Cpx (En_{40-42}) and Opx (En_{68}) were generated at 1000ºC, 400 MPa, 6±0.7 wt % H_2O_{melt}, ~NNO, i.e., at depths corresponding to 15-16 km for a rock density of 2500-2700 kg/m^3. In contrast, the Mg-rich pyroxenes and Ca-rich Pl crystallized at somewhat lower temperatures (975ºC), shallower depths (200 MPa, corresponding to 8-10 km), for a lower H_2O_{melt} (5±0.7 wt %) and under more oxidized conditions (fO_2~NNO+1.7). These estimates are in good agreement with tomography data of Molina *et al.* (2005) and with previous thermo-barometric estimates, which suggested ponding levels for the andesitic magma at 200-250 MPa (Samaniego *et al.*, 2011). Our estimates for the deep crystallization stage (400 MPa, i.e. ~15-16 km deep) encompass those inferred from INSAR which suggest the presence of a large magmatic body at depths of 12-15 km below Tungurahua (Champenois *et al.* 2014). In contrast, melt inclusions in minerals such as Ol, Cpx, Opx and Pl have suggested pressures as low as ≤ 100 MPa (4 km depth) for the andesitic body (Myers *et al.* 2014). However, as stressed above, at these pressures, neither the natural mineral assemblage nor the phase compositions have been experimentally reproduced, which suggest that there is no permanently established magma reservoir in this pressure range. Our single Fe-Ti oxide temperature estimate (1000ºC) and those of Samaniego *et al.* (2011) based on clinopyroxene-orthopyroxene equilibrium (1007 ± 14 ºC), encompass the temperatures inferred experimentally for the andesitic magma. It should be noted that the range of melt water contents predicted experimentally (5-6 wt % H_2O) implies that the Tungurahua magmas are quite water-rich. This observation is in broad agreement with the elevated H_2O contents (up to 4 wt %) of melt inclusions in $Fo_{80\pm2}$ olivine which are in equilibrium with 54-57 wt % SiO_2 melts (Myers *et al.*, 2014).

An open magmatic system

Mineralogical evidence for two different superimposed crystallization environments in the andesite magma is consistent with Tungurahua behaving as an open magmatic system. According to this model, the 200 MPa ponding level would be periodically recharged by magma batches coming from the 400 MPa reservoir. Ultimately, all magmas would originate from the deep storage level at 15-16 km depth. We have tested further the model by checking that the Ca- and Mg-rich rims on plagioclase and pyroxene crystals cannot originate from mixing with a foreign mafic (i.e., basaltic or basaltic andesitic) melt. To do so, the distribution of Fe* content in Pl, as proposed by Ruprecht & Wörner (2007) has been used: a rimward increase of both Ca and Fe* in Pl crystals would suggest a mixing process involving a mafic magma. In our case, the An_{65-70} rims have FeO* contents (~0.5-0.6 wt %) similar to the $An_{50\pm5}$ cores (Table 1, Supplementary Data Appendix natural; Samaniego *et al.*, 2011) which rules out the foreign basaltic magma hypothesis to explain the Ca and Mg-rich rim compositions. This conclusion is consistent with the lack of basaltic magmas at Tungurahua. Magmas with the highest Ca/Na (able to crystallize An-rich plagioclase) are represented by basaltic andesitic whole-rocks and melt inclusions whose SiO_2 contents are 54 wt % minimum (Fig. 1c; Hall *et al.* 1999; Samaniego *et al.* 2011; Myers *et al.* 2014).

Origin of olivine in the andesitic magma

One striking feature of 2006 samples and andesitic products emitted at Tungurahua in general is the presence of normally zoned Ol crystals ($Fo_{80\pm2}$ to $Fo_{75\pm2}$), all of them displaying clear evidence for disequilibrium as marked by resorbed margins and narrow rims with Opx (En_{71}), Pl and Fe-Ti oxides (Supplementary Data Appendix natural; Samaniego *et al.*, 2011; Myers *et al.*, 2014). This suggests either that Ol crystals are not in equilibrium with the interstitial melt (witnessing the injection of a foreign basaltic magma) or that Ol was once part of the stable phenocryst assemblage of the mafic andesitie magma, but conditions in the feeding system evolved to make it unstable, reacting to Opx.

Concerning the first hypothesis, the involvement of a foreign basaltic magma is not consistent with the previously discussed Ca and Fe* Pl zonation data. If the MI data in Ol are examined, it appears that melts trapped in $Fo_{80\pm2}$ olivines have SiO_2 between 54-58 wt % (Figs. 1c, 4c; Myers *et al.*, 2014) and those in $Fo_{75\pm2}$ have 60-63 wt % SiO_2 (Figs. 1c; 4c). The Mg-poor olivine group ($Fo_{75\pm2}$) is therefore associated with andesitic and the Mg-rich group with basaltic andesite melts (Fig 4c). Despite their wide SiO_2 range (54-58 wt %), the basaltic andesite MI have similar and rather low Mg# (~Mg# = 40; Mg# = 100*MgO/(MgO+FeO*); Fig 1d). Thus, there is no indication from the MI data for the existence of primitive basaltic liquids and so the presence of olivine xenocrysts appears very unlikely. In contrast, the natural olivine compositions have been successfully reproduced at equilibrium with liquids from 60 and up to 64 wt % SiO_2 (Fig. 4c). Therefore, experimental results indicate that the second hypothesis is viable, as long as water-rich conditions prevail ($H_2O_{melt} > 5$ wt %; Fig. 3, 4a). However, conditions (in particular depths) of crystallization of Ol crystals remain to be determined and the mechanism of Ol resorption clarified.

In the experiments, $Fo_{80\pm2}$ Ol crystallized under water-saturated conditions at 100 MPa (charge T54), 200 MPa (T45b, T23, T10) and 400 MPa (T33; Fig. 3; Table 3). At 100 MPa, Ol is at equilibrium with a Cpx (Wo_{40}) depleted in Ca compared to the Mg-rich pyroxene population ($Wo_{43\pm0.5}$). This rules out 100 MPa as the crystallization pressure for the $Fo_{80\pm2}$ Ol. Ol crystallized at higher pressures (200 and 400 MPa) coexists with a Cpx that encompasses the natural compositions ($En_{46\pm1}Fs_{11\pm1}Wo_{43\pm0.5}$, Mg# = 81±2, Table 4). However, our phase equilibrium results indicate that Ol stability is drastically reduced when pressure is increased from 200 to 400 MPa (Fig. 3e). At 400 MPa, olivine is only present at 1000ºC for ~10 wt % H_2O_{melt} (Fig. 3, charge 33), i.e., for an H_2O_{melt} range that exceeds our estimates for the early crystallization stage. This observation, together with the lack of isolated homogenous $Fo_{80\pm2}$ crystals in the erupted products, point towards an origin at P < 400 MPa for the $Fo_{80\pm2}$ olivines, most probably at pressures of ~200 MPa. One additional indication comes from normal zoning in natural Ol. According to our results, compositions of Mg-poor Ol rims ($Fo_{75\pm2}$) can form at 975ºC, 200 MPa, NNO+2 (run T24; Fig. 4a). The available experimental evidence therefore implies that Ol crystallizes as a stable phenocryst phase in the Tungurahua plumbing system.

To explain the resorption of the $Fo_{80\pm2}$ Ol crystallized at 200 MPa, it should be reminded that Tungurahua is characterised by the presence of a continuous degassing plume (Fig. 1d) and by a high eruption rate (several events per year since 1999; IGEPN internal reports). Such a permanent degassing regime, perhaps maintained by the recurrent partial emptying of the shallow reservoir and, or, the conduit during eruptions, could slightly lower the H_2O content inferred for the 200 MPa magma ponding level (5 wt % H_2O_{melt}; Fig. 3a), shifting the system outside the olivine stability field (Fig. 3a). In the 200 MPa phase diagram, the field for shallow pre-eruptive conditions straddles the Ol stability curve so that a temperature drop < 975°C or an fO_2 increase above NNO+2 would also lead to Ol resorption

(Fig. 3a). The transition from an Ol-bearing to an Ol-free phase assemblage has been experimentally simulated at 975°C, 200 MPa between charges T24 and T25 (Table 2). Opx in the Ol-free charge T25 is En_{75}, close to Opx compositions in Ol reaction rims (En_{71-72}; Supplementary Data Appendix natural; Samaniego *et al*., 2011; Myers *et al*., 2014). Note also that the co-crystallizing Cpx is $En_{44}Fs_{14}Wo_{41}$, Mg# = 75 (charge T25; Table 4), a composition that occurs in the natural andesite (Fig. 2a) and thus strengthens our interpretation that Ol resorption takes place in the plumbing system at pressures close to 200 MPa.

Sequence of events for the July-August 2006 eruption

By combining our estimates of pre-eruptive conditions for the andesite magma and its petrological attributes, below we propose the following sequence of events for the 2006 Tungurahua eruptions.

A significant volume of basaltic andesite magma was first stored at 400 MPa (15-16 km depth), 1000ºC, fO_2~NNO and *ca*. 6 wt % H_2O_{melt}. Ponding of the magma under these conditions led to the crystallization of the main mineral assemblage Pl ($An_{50\pm5}$), Cpx (En_{40-42}), Opx (En_{68}), Mt (Mg#5), and Ilm (Fig. 10, 1st step). Intrusion of a new batch of mafic andesite into the 400 MPa reservoir might have triggered magma ascent to shallower depths (200 MPa or 8-10 km; Fig 10, 2nd -3rd steps). Crystallization and subsequent cooling (from 1000ºC to 975ºC) of the system at this level (200 MPa) produced first the $Fo_{80\pm2}$ olivine, the Mt and the Ca- and Mg-rich rims on Pl and Cpx; and second, the low-Mg Ol, the Ca- and Mg-rich Pl and Opx respectively. The excess H_2O generated during crystallization was then outgassed, which could have increased the fO_2 of the magma from NNO+0.13 to NNO+1.7 (i.e., Burgisser *et al*., 2008; Fig. 10, 4th step), thus destabilizing the few Ilm crystals present (Fig. 3a). At this point, we cannot rule out the possibility that crystallization or degassing of the magma overpressurized the system to trigger an eruption (for instance the July 2006 events; Fig. 10 5th step) since the volcanic products emitted during July and August 2006 share similar petrological and chemical features (Samaniego *et al*., 2011). The permanent degassing (from 6 to 5 wt % H_2O_{melt}; Figs 3a,c) or the partial emptying of the reservoir by subsequent July eruptions, could have slightly changed the H_2O content of the 200 MPa reservoir and affected olivine stability (Fig 3). Crossing of the olivine-out curve promoted olivine resorption to Opx (En_{71-72}) reaction rims (Fig. 3, run T25).

Finally, after a period of quiescence, a new batch of hot, volatile-rich, andesite magma (coming from 400 MPa and containing the same phase assemblage and mineral compositions as the first batch), again intruded the andesite residing at 200 MPa, triggering a new eruption (August 2006; Fig 10, 6th-7th steps). Importantly, the time difference between injection and eruption must have been short, preventing thorough chemical mixing between the intruding and resident andesitic batches, so as to preserve the two crystal populations crystallized at 200 and 400 MPa. The above model proposed for the July-August 2006 Tungurahua events is consistent with the open-system, highly dynamic and high eruption frequency characteristic of this volcano during past and present times (Hall *et al*. 1999; Le Pennec *et al*., 2008; Samaniego *et al*., 2011, IGEPN internal reports.

CONCLUSIONS

The combination of new petrological and phase equilibrium data obtained on the 2006 eruptive products of Tungurahua allow us to determine the storage conditions of the andesitic magmas emitted during this eruption, as well as to infer the structure of the plumbing system below the volcano. Our results suggest that the Tungurahua andesitic magmas are hot (1000-975ºC) and water-rich (5-6 wt%). These characteristics seem to be a constant feature at this volcano since, historically, Tungurahua has emitted rather homogeneous andesitic magmas.

The July-August 2006 plumbing system was characterised by two magma reservoirs located at 15-16 km (400 MPa) and 8-10 km (200 MPa), both simultaneously active during this time period. Magmas stored at 400 MPa interacted with those residing at 200 MPa, resulting in a complex inverse zonation of the phenocrysts. Moreover, the interaction between these two reservoirs played an important role in controlling the eruptive dynamics of the system. Magmas residing in the 200 MPa reservoir were slightly colder and more degassed than those in the 400 MPa reservoir, which were hotter and water-rich. The shallow reservoir fed the strombolian-vulcanian and effusive activity, whereas the more explosive (subplinian) events were driven by the incoming of the deeper magmas from the 15-16 km depth reservoir (400 MPa). How detailed petrological characterization can lead to a better understanding of the eruptive dynamics is demonstrated by our work. Finally, results presented in this paper contribute to the experimental characterization of mafic members of the adakitic series and are potentially applicable to other geochemically similar systems in the Northern Volcanic Zone of Ecuador.

ACKNOWLEDGEMENTS

The ISTO group thanks I. Di Carlo for the technical support with SEM and EMPA and Daniel Andrade, Silvana Hidalgo, Patricia Mothes and Mario Ruíz for scientific discussions about Tungurahua. Reviews from I. Smith and two anonymous reviewers improved the quality of the manuscript. We also thank for the comments and Editorial handling of editors J. Gamble and M. Wilson

FUNDING

This work was funded by Prometeo program (I. M.), VUELCO project and Equipex-Planex ANR-11-EQPX-0036, INSU-CNRS ALEA.

REFERENCES

Almeev, R.R., Holtz, F., Ariskin, A.A. & Kimura, J-I. (2013). Storage conditions of Bezymianny Volcano parental magmas: results of phase equilibria experiments at 100 and 700 MPa. *Contributions to Mineralogy and Petrology* **166**, 1389–1414.

Andújar, J. & Scaillet, B. (2012a). Experimental constraints on parameters controlling the difference in the eruptive dynamic of phonolitic magmas: the case from Tenerife (Canary Islands). *Journal of Petrology* **53**, 1777-1806.

Andújar J, Scaillet B (2012b) Relationships between pre-eruptive conditions and eruptive styles of phonolite–trachyte magmas. *Lithos* **152**, 122-131

Andújar, J., Costa, F. & Scaillet, B. (2013). Storage conditions and eruptive dynamics of central versus flank eruptions in volcanic islands: the case of Tenerife (Canary Islands, Spain). *Journal of Volcanology and GeothermalResearch*, **260**, 62-790 doi:10.1016/j.jvolgeores.2013.05.004.

Andújar, J., Scaillet, B., Pichavant, M. & Druitt, T.H. (2015); Differentiation Conditions of a Basaltic Magma from Santorini, and its Bearing on the Production of Andesite in Arc Settings. *Journal of Petrology* **56**,765-794.

Arellano S., Hall, M.L., Samaniego, P., Le Pennec, J.L., Ruiz, G., Molina, I. & Yepes, H. (2008). Degassing patterns of Tungurahua volcano, Ecuador, during the 1999–2006 eruptive period deduced from spectroscopic remote measurements of SO_2 emissions. *Journal of Volcanology and Geothermal Research* **176**,151–162

Bacon, C.R. & Hirschmann M.M: (1988). Mg/Mn partitioning as a test for equilibrium between coexisting Fe-Ti oxides. *American Mineralogist* **73**, 57-61.

Barclay, J. & Carmichael, I. S. E. (2004). A hornblende basalt from western Mexico: water-saturated phase relations constrain a pressure–temperature window of eruptibility. *Journal of Petrology* **45**, 485–506.

Berndt, J., Koepke, J. & Holtz, F. (2005). An experimental investigation of the influence of water and oxygen fugacity on differentiation of MORB at 200 MPa. *Journal of Petrology* **46**, 135-167.

Biggs, J., Mothes, P., Ruíz, M., Amelung, F., Dixon, T.H., Baker, S. & Hong, S.H. (2010). Stratovolcano growth by co-eruptive intrusion: The 2008 eruption of Tungurahua Ecuador. *Geophysical Research letters* **37**, L21302

Blatter, D.L. & Carmichael, I.E.S. (1998). Plagioclase-free andesites from Zitácuaro (Michoacán), Mexico: petrology and experimental constraints. *Contributions to Mineralogy and Petrology* **132**, 121–138.

Bourdon, E., Eissen, J-P, Monzier, M., Robin, C., Martin, H. , Cotten, J. & Hall, M.L. (2002 a). Adakite-like Lavas from Antisana Volcano (Ecuador): Evidence for Slab Melt Metasomatism Beneath the Andean Northern Volcanic Zone. Journal of Petrology 43, 199-207.

Bourdon, E., Eissen, J-P, Gutscher, M-A., Monzier, M., Hall, M.L. & Cotton, J. (2002b). Magmatic response to early aseismic ridge subduction: the Ecuadorian margin case (South America). *Earth and Planetary Science Letters* **205**, 123-138

Burgisser, A. & Scaillet, B. (2007). Redox evolution of a degassing magma rising to the surface. *Nature* **445**, 194-197.

Burnham, C.W., Holloway, J.R., Davis, N.F. (1969). Thermo-dynamic properties of water

to 1000 °C and 10000 bar. Geological Society of America, Special Paper 132, 1–96.

Castro, J. M. & Mercer, C. (2004). Microlite textures and volatile contents of obsidian from Inyo volcanic chain, California. *Geophysical Research Letters* **31**, L18605.

Champenois, J., V. Pinel, S. Baize, L. Audin, H. Jomard, A. Hooper,A. Alvarado & H. Yepes (2014). Large-scale inflation of Tungurahua volcano (Ecuador) revealed by Persistent Scatterers SAR interferometry. ,Geophysical Research Letters **41**,doi:10.1002/2014GL060956.

Costa, F., Scaillet, B. & Pichavant, M. (2004). Petrological and experimental constraints on the pre-eruption conditions of Holocene dacite fromVolcan San Pedro (368S,Chilean Andes) and the importance of sulphur in silicic subduction-related magmas. *Journal of Petrology* **45**, 855-881.

Deer, W.A.; Howie, R.A. & Zussman, J. (1972). Rock forming minerals: Framework silicates 4, 435 pp.

Drummond, M.S. & Defant, M.J. (1990). Derivation of some modern arc magmas by melting of young subducted lithosphere. *Nature* **347**, 662 - 665*Devine, J. D., Gardner, J. E., Brack, H. P., Layne, G. D. & Rutherford, M. J. (1995). Comparison of microanalytical methods for estimating H2O contents of silicic volcanic glasses. *American Mineralogist* **80**, 319-328.

Di Carlo, I., Pichavant, M., Rotolo, S.G. & Scaillet, B. (2006). Experimental crystallization of a High-K arc basalt: the golden pumice, Stromboli volcano (Italy). *Journal of Petrology* **47**, 1317-1343.

Erdmann, S., Martel, C., Pichavant, M. & Kushnir, A. (2014) Amphibole as an archivist of magmatic crystallization conditions: problems, potential, and implications for inferring magma storage prior to the paroxysmal 2010 eruption of Mount Merapi, Indonesia. *Contribution to Mineralogy and Petrology* **167***, 1016, DOI 10.1007/s00410-014-1016-4.*

Eychenne, J., Le Pennec, J.L., Ramón, P.& Yepes, H. (2013). Dynamics of explosive paroxysms at open-vent andesitic systems: high-resolution mass distribution analyses of the 2006 Tungurahua fall deposit (Ecuador). *Earth and Planetary Science Letters* **361**, 343-355.

Feig, S. T. Æ Ju¨ rgen Koepke, J. & Snow, J.E. (2006). Effect of water on tholeiitic basalt phase equilibria: an experimental study under oxidizing conditions. *Contributions to Mineralogy and Petrology***152**,611–638

Freise, M., Holtz, F., Nowak, M., Scoates, J. S. & Strauss, H. (2009). Differentiation and crystallization conditions of basalts from the Kerguelen large igneous province: an experimental study. *Contributions to Mineralogy and Petrology* **158**, 505-527.

Garrison, J.M. & Davidson, J.P. (2003). Dubious case for slab melting in the Northern volcanic zone of the Andes. *Geology* **31**, 565–568

Hall, M.L., Robin, C., Beate, B., Mothes, P. & Monzier, M. (1999). Tungurahua Volcano, Ecuador: structure, eruptive history and hazards. *Journal of Volcanology and Geothermal Research* **91**, 1-21.

Hall, M.L., Steele, A.L., Mothes, P.A. & Ruiz, M.C. (2013). Pyroclastic density currents (PDC) of the 16-17 August 2006 eruptions of Tungurahua volcano, Ecuador: geophysical registry and characteristics. *Journal of Volcanology and Geothermal Research* **265**, 78-93.

Hidalgo, S., Gerbe. M.C., Martin, H., Samaniego, P. & Bourdon, E. (2012). Role of crustal and slab components in the Northern Volcanic Zone of the Andes (Ecuador) constrained by Sr–Nd–O isotopes. Lithos 132-133 180–192.

Jaupart, C. & Allègre,C.J. (1991). Gas content, eruption rate and instabilities of eruption regime in silicic volcanoes. *Earth and Planetary Science Letters* **102**, 413-429.

Kelemen, P.B., Hanghøj, K. & Greene, A.R. (2014). One View of the Geochemistry of Subduction-Related Magmatic Arcs, with an Emphasis on Primitive Andesite and Lower Crust. Treatise on Geochemistry 2nd Edition 749-805. http://dx.doi.org/10.1016/B978-0-08-095975-7.00323-5

Kress, V. C. & Carmichael, I. S. E. (1991). The compressibility of silicate liquids containing Fe2O3 and the effect of composition, temperature, oxygen fugacity and pressure on their redox states. *Contributions to Mineralogy and Petrology* **108**, 82–92.

Kumagai, H., Palacios, P., Ruíz, M., Yepes, H. & Kozono, T. (2011). Ascending seismic source during an explosive eruption at Tungurahua volcano, Ecuador. *Geophysical Research letters* **38**, L01306, doi:10.1029/2010GL045944, 2011

Leake, B. E., Woolley, A. R., Arps, C. E. S., et al. (1997). Nomenclature of amphiboles: report of the subcommittee on amphiboles of the International Mineralogical Association Commission on New Minerals and Mineral Names. *Mineralogical Magazine* **61**, 295–321.

Le Bas, M.J. & Streckeisen, A.L. (1991). The IUGS systematics of igneous rocks. *Journal of the Geological Society of London* **148**, 825–833.

Le Pennec, J.-L., Jaya, D., Samaniego, P., Ramón, P., Moreno Yánez, S., Egred, J. & Van der Plicht, J. (2008). The AD 1300–1700 eruptive periods at Tungurahua volcano, Ecuador, revealed by historical narratives, stratigraphy and radiocarbon dating, *Journal of Volcanology and Geothermal Research* **176**, 70-81. doi:10.1016/j.jvolgeores.2008.05.019

Le Pennec, J.L., de Saulieu, G., Samaniego, P., Jaya, D. & Gailler, L. (2013). A devastating Plinian eruption at Tungurahua volcano reveals formative occupation at ~1100 cal BC in Central Ecuador. *Radiocarbon* **55**, 1199-1214.

Le Pennec, J.L., Ramon, P., Robin, C. & Almeida, E. (2016). Combining historical and 14C data to assess pyroclastic density current hazards in Baños city near Tungurahua volcano (Ecuador*). Quaternary International* **394**, 98-114

Libourel, G. (1999). Systematics of calcium partitioning between olivine and silicate melt: implications for melt structure and calcium content of magmatic olivines. *Contributions to Mineralogy and Petrology* **136**, 63–80

López, C., Blanco, M. J., Abella, R. et al. (2012).Monitoring the unrest of El Hierro (Canary Islands) before the onset of the 2011 submarine eruption. Geophysical Research Letters 39, L13303, doi:10.1029/2012GL051846.

Martel C. (2012). Eruption dynamics inferred from microlite crystallization experiments: Application to Plinian and dome-forming eruptions of Mt. Pelée (Martinique, Lesser Antilles). *Journal of Petrology* **53**, 699-725.

Martel, C., Pichavant, M., Bourdier, J.L., Traineau, H., Holtz, F., Scaillet, B., 1998. Magma storage conditions and control of eruption regime in silicic volcanoes: experimental evidence from Mt. Pelée. Earth and Planetary Science Letters 156, 89–99.

Martel, C., Pichavant, M., Holtz, F. & Scaillet, B. (1999). Effects of fO_2 and H_2O on andesite phase relations between 2 and 4 kbar. *Journal of Geophysical Research* **104**, 29,453-29,470.

Martel, C. & Schmidt, B.C. (2003). Decompression experiments as an insight into ascent rates of silicic magmas. *Contributions to Mineralogy and Petrology* **144**, 397–415

Martí, J., Castro, A., Rodríguez, C., Costa, F., Carrasquilla, S., Pedreira, R. & Bolos, X., (2013). Correlation of magma evolution and geophysical monitoring during the 2011–2012 El Hierro (Canary Islands) submarine eruption: *Journal of Petrology*, **54**, 1349–1373, doi:10.1093/petrology/egt014.

Molina, I., Kumagai, H. & Yepes, H. (2004) Resonances of a conduit triggered by repetitive injections of an ash-laden gas. *Geophysical Research Letters* **31**, 1-4, doi:10.1029/2003GL018934.

Molina, I., Kumagai, H., Le Pennec, J.L. & Hall, M. (2005). Three-dimensional P-wave velocity structure of Tungurahua Volcano, Ecuador. *Journal of Volcanology and Geothermal Research* **147**, 144-156.

Moore, G. & Carmichael. I.E.S. (1998). The hydrous phase equilibria (to 3 kbar) of an andesite and basaltic andesite from western Mexico: constraints on water content and conditions of phenocryst growth . *Contributions to Mineralogy and Petrology* **130**, 304-319

Morimoto N. (1989). Nomenclature of pyroxenes. Subcomitee on pyroxenes. Commission on new minerals and mineral names. *Canadian Mineralogist* **27**, 143-156.

Myers, M-L., Geist, D.J., Rowe, M.C., Harpp K.S., Wallace, P.J. & Dufek, J. (2014). Replenishment of volatile-rich mafic magma into a degassed chamber drives mixing and eruption of Tungurahua volcano. *Bulletin of Volcanology* **76**, 872-

Papale, P., Moretti, R. & Barbato, D. (2006). The compositional dependence of the saturation surface of H_2O+CO_2 fluids in silicate melts. *Chemical Geology* **229**, 78–95

Pichavant M., Martel C., Bourdier J.-L. & Scaillet B. (2002). Physical conditions, structure and dynamics of a zoned magma chamber: Mt. Pele´e (Martinique, Lesser Antilles arc). *Journal of Geophysical Research* **107**, doi:10.1029/ 2001JB000315

Pichavant, M. & Macdonald, R. (2007). Crystallization of primitive basaltic magmas atcrustal pressures and genesis of the calc-alkaline igneous suite: experimental evidence from St. Vincent, Lesser Antilles arc. *Contributions to Mineralogy and Petrology* **154**, 535-558.

Prouteau, G & Scaillet, B. (2003). Experimental Constraints on the Origin of the 1991 Pinatubo Dacite. Journal of Petrology **44**, 2203-2241.

Pownceby, M.I. & O'Neill, H. St.C. (1994). Thermodynamic data redox reactions at high temperatures.III. Activity-composition relations in Ni-Pd alloys from EMF measurements at 850-1250 K and calibration of the NiO+Ni-Pd assemblage a redox sensor. *Contributions to Mineralogy and Petrology* **116**, 327-339.

Ridolfi, F. & Renzulli, A. (2012). Calcic amphiboles in calcalkaline and alkalinemagmas: thermobarometric and chemometric empirical equations valid up to 1130ºC and 22GPa. *Contributions toMineralogy and Petrology* **163**, 877–895.

Robie, R.A., Hemingway, B.S. & Fisher, J.R. (1979). Thermodynamic properties of minerals and related substances at 298.15 K and 1 bar (105 pascals) pressure and at higher temperatures. *US Geological Survey Bulletin* **1452**, 456.

Ruprecht, P. & Wörner, G. (2007). Variable regimes in magma systems documented in plagioclase zoning patterns: El Misti stratovolcano and Andahua monogenetic cones. *Journal of Volcanology and Geothermal Research* **165**, 142–162.

Rutherford, M.J. (2008). Magma ascent rates. Reviews in Mineralogy **69**, 241-271.

Samaniego, P., Martin, H., Monzier, M., Robin, Fornari, M., Eissen, J-P. & Cotton, J. (2005).Temporal Evolution of Magmatism in the Northern Volcanic Zone of the Andes: The Geology and Petrology of Cayambe Volcanic Complex (Ecuador). Journal of Petrology **46**, 2225-2252.

Samaniego, P., Le Pennec, J.L., Robin, C. & Hidalgo, S. (2011). Petrological analysis of the pre-eruptive magmatic process prior to the 2006 explosive eruptions at Tungurahua volcano (Ecuador). *Journal of Volcanology and Geothermal Research* **199**, 69-84. doi:10.1016/j.jvolgeores.2010.10.010

Sauerzapf, U., Lattard, D., Burchard, M. & Engelmann, R. (2008). The titanomagnetite ilmenite equilibrium: new experimental data and thermo-oxybarometric application to the crystallization of basic to intermediate rocks. *Journal of Petrology* **49**, 1161–1185.

Scaillet, B., Pichavant, M. & Roux, J. (1995). Experimental crystallization of leucogranites magmas. *Journal of Petrology* **36**, 663-705.

Scaillet, B. & Evans, B. W. (1999). The 15 June 1991 eruption of Mount Pinatubo. I. phase

equilibria and Pre-eruption P-TfO$_2$-aH$_2$O. Journal of Petrology 40, 381–411.

Scaillet, B. & Macdonald, R. (2006). Experimental and thermodynamic constraints on the sulphur yield of peralkaline and metaluminous silicic flood eruptions. *Journal of Petrology* **47**, 1413-1437.

Scaillet, B., Pichavant, M. & Cioni, R. (2008). Upward migration of Vesuvius magma chamber over the past 20,000 years. ***Nature*** 455, 216–219.

Sisson, T. W. & Grove, T. L. (1993). Experimental investigations of the role of H2O in calc-alkaline differentiation and subduction zone magmatism. *Contributions to Mineralogy and Petrology* **113**, 143–166.

Stormer, J.C. & Nichols, J. (1978). XLFRAC: a program for the interactive testing of magmatic differentiation models. *Computers & Geoscience* **4**, 143–159.

Sparks, R. S. J., Barclay, J., Jaupart, C., Mader, H. M. & Phillips, J. C. (1994). Physical aspect of magmatic degassing I. Experimental and theoretical constraints on vesiculation. In: Carroll, M. R. & Taylor, J. R., Wall, V.J. & Pownceby, M. I. (1992). The calibration and application of accurate redox sensors. *American Mineralogist* **77**, 284-295.

Wood, B.J., & Turner, S. (2009). Origin of primitive high-Mg andesite: Constraints from natural examples and experiments. *Earth and Planetary Science Letters*, **283**, 59–66.

FIGURE CAPTIONS

Figure 1**. (a)** Location of the Ecuadorian volcanic belt and (b) digital elevation model of Tungurahua showing the distribution of the July-August 2006 products (after Samaniego *et al.* 2011); (c) Mg# melt vs SiO$_2$ content of volcanic rocks, melt inclusions (MI) and starting material (stars are for bulk-rock and glass composition of Table 1). Data from Hall *et al.* (1999), Samaniego *et al.* (2011), Myers *et al.* (2014) and this work. (d) Photograph of Tungurahua summit showing permanent degassing plume (B. Scaillet)

Figure 2. Representative compositional zoning profiles of phenocrysts in the August 2006 andesite. (a) plagioclase (b) clinopyroxene and orthopyroxene.

Figure 3. Isobaric phase relationships of the August 2006 Tungurahua andesite. (a) 200 MPa-NNO+1 and NNO+2, (b) 100 MPa-NNO+1 and NNO+2, (c) 400 MPa-NNO+1, (d) 400 MPa-NNO+2, (e) isothermal section at 1000ºC - NNO+1, (f) isothermal section at 1000ºC-NNO+2; In (a) and (b) purple lines show the mineral-in curves at NNO+2. In (c) Ol is stable in one charge. Grey-shaded boxes bound the inferred pre-eruptive conditions of the natural rock.

Figure 4. Compositions of experimental olivines (Fo content in mol %) versus (a) H_2O (wt%) in co-existing melt; (b) CaO (wt%) in olivines; (c) Fo content in mol % versus SiO_2 content in co-existing melt. Orange and red circles correspond to the Fo content and Melt Inclusion SiO_2 content of the 2006 and 2010 natural products of Myers *et al*. (2014). Numbers next to the symbols in the legend indicate pressure (MPa) and prevailing *fO2* conditions.

Figure 5. Compositional variation of experimental clinopyroxenes. (a) Mg#, (b) En content (mol%), (c) Fs content (mol%) and (d) Wo content (mol%) of the clinopyroxene as function of melt H_2O content (wt%). Numbers next to symbols in the legend indicate pressure (MPa) and prevailing *f*O2 conditions.

Figure 6. Compositional variation of experimental orthopyroxenes. (a) Mg#, (b) En content (mol%), (c) Fs content (mol%) as functions of melt H_2O content (wt%). Numbers next to symbols in the legend indicate pressure (MPa) and prevailing *fO2* conditions.

Figure 7. Compositional variation of the experimental plagioclase. (a) An content (mol %) versus H_2O_{melt} (wt%); (b) Ab content (mol %) versus H_2O_{melt}, and (c) Or content (mol %) versus H_2O_{melt} (wt%). Numbers next to symbols in the legend indicate pressure (MPa) and prevailing *f*O2 conditions.

Figure 8. Compositional variation of experimental magnetite. (a) Mg# and (b) TiO_2 (wt %) content as function of melt H_2O, (c) TiO_2 (wt %) content as function of Mg#. The star shows the magnetite population observed in the 2006 andesite sample. Legend as in previous figures.

Figure 9. Experimental glass compositional variations of major and minor oxides *versus* water content in the melt. Grey horizontal bar shows the natural melt composition (Table 1). Legend as in previous figures.

Figure 10. Schematic cartoon summarizing the processes proposed to have occurred prior the August 2006 eruption. (1) ponding at 400 MPa of the andesitic magma and crystallization of the main mineral assemblage, (2) injection of new magma into the 400 MPa reservoir ?, (3) magma rising from 400 to 200 MPa level, (4) cooling down, formation of Mg-Ca-rich rims and outgassing of the system, (5) over-pressurization and eruption (July 2006), (6) input of a new magma batch into the 200 MPa reservoir, mixing and (7) eruption in August 2006.

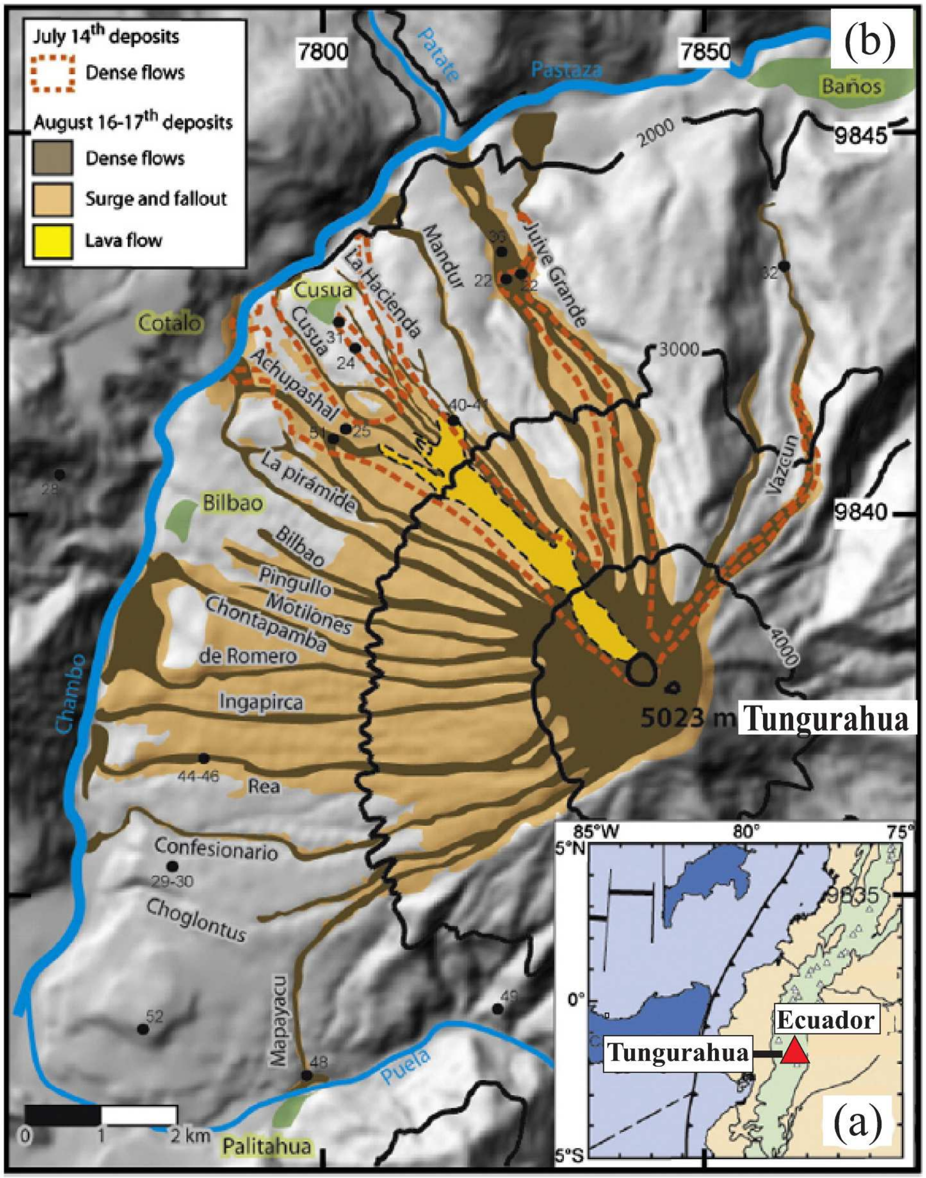

Fig. 1a,b

256x308mm (300 x 300 DPI)

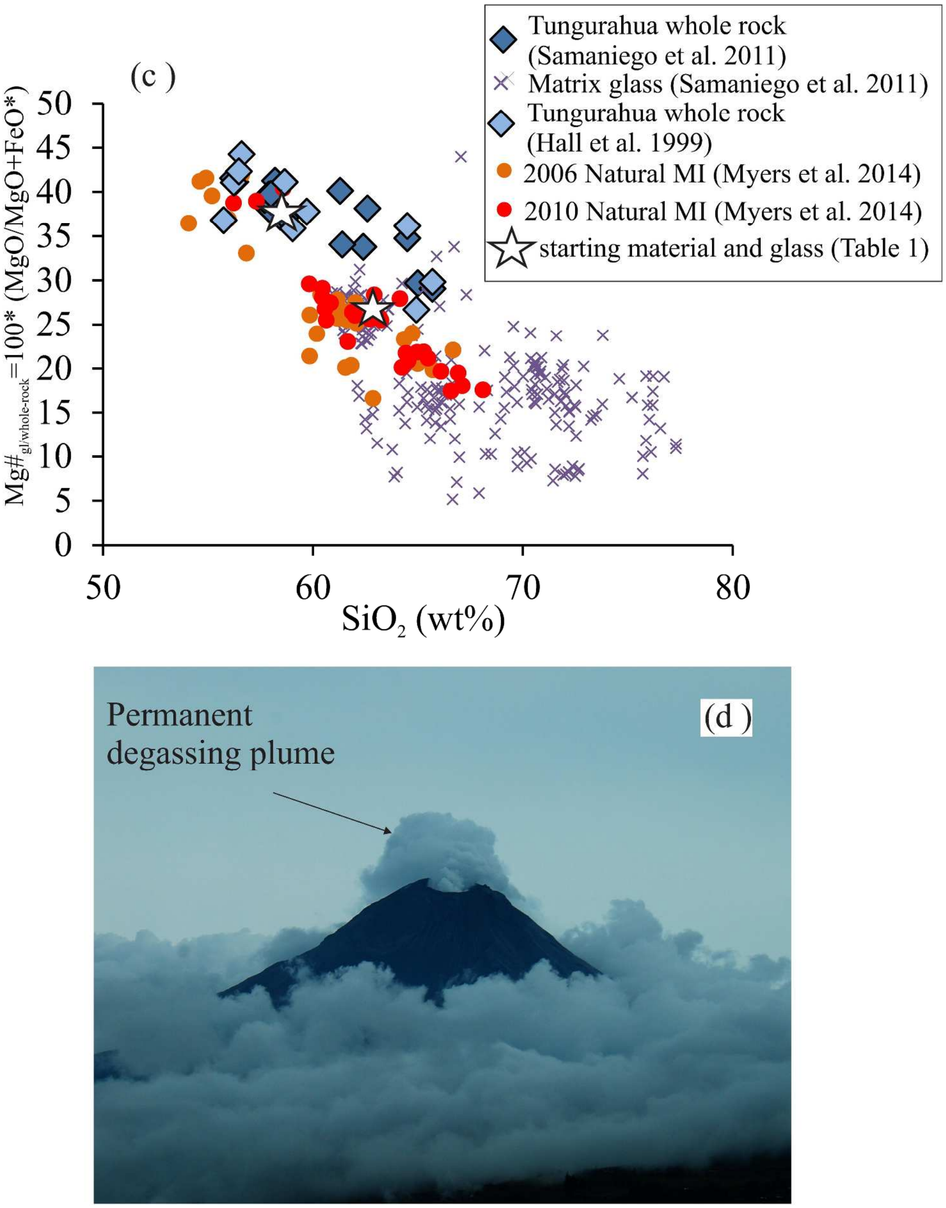

279x356mm (300 x 300 DPI)

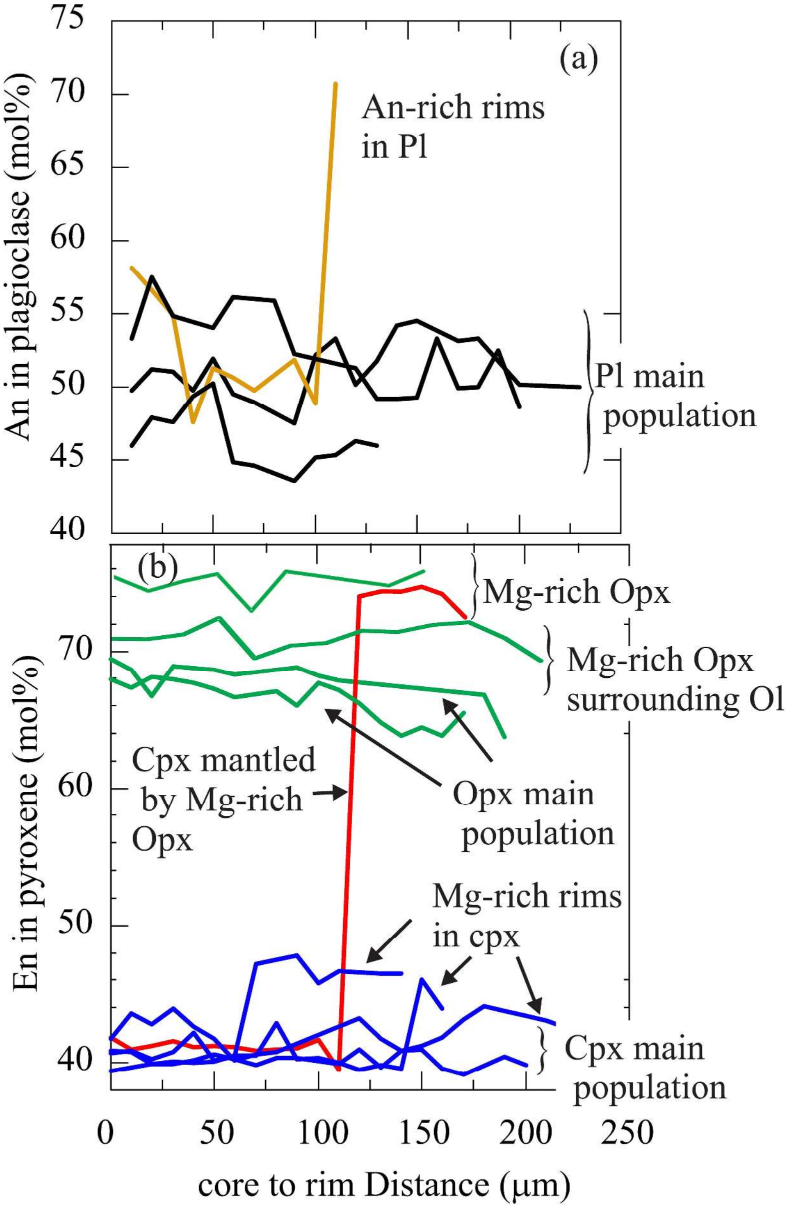

282x433mm (300 x 300 DPI)

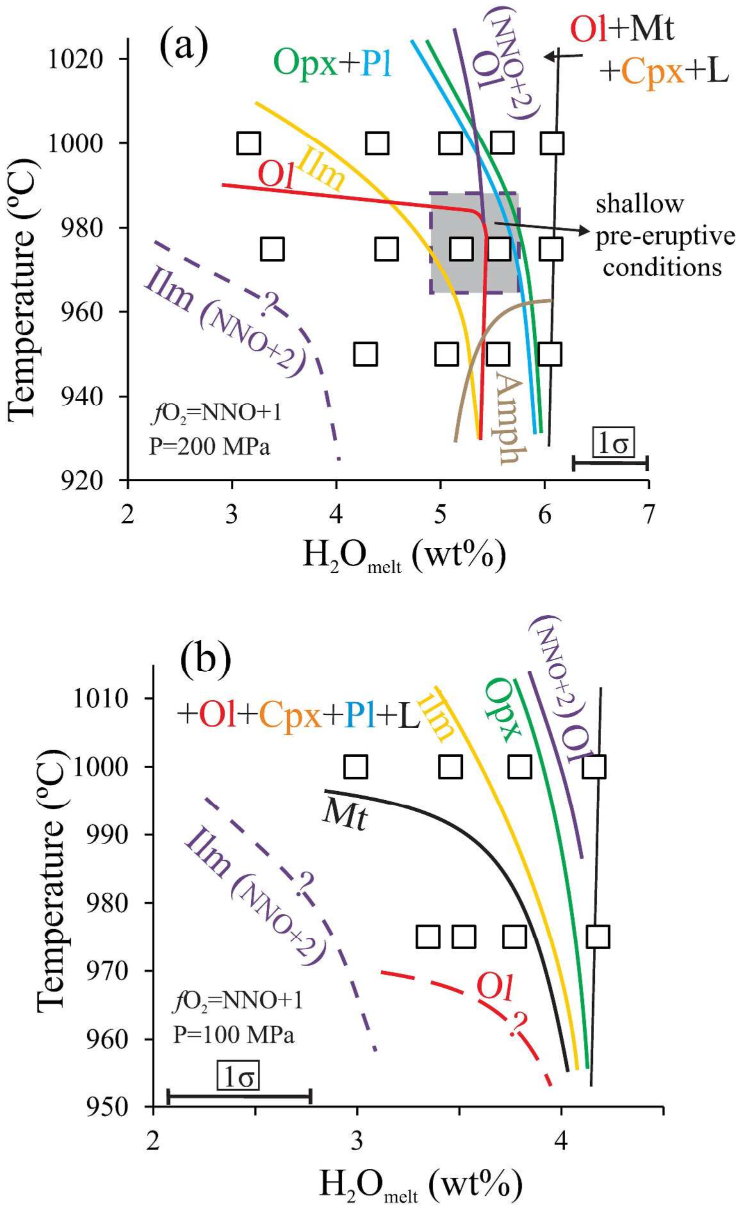

264x435mm (300 x 300 DPI)

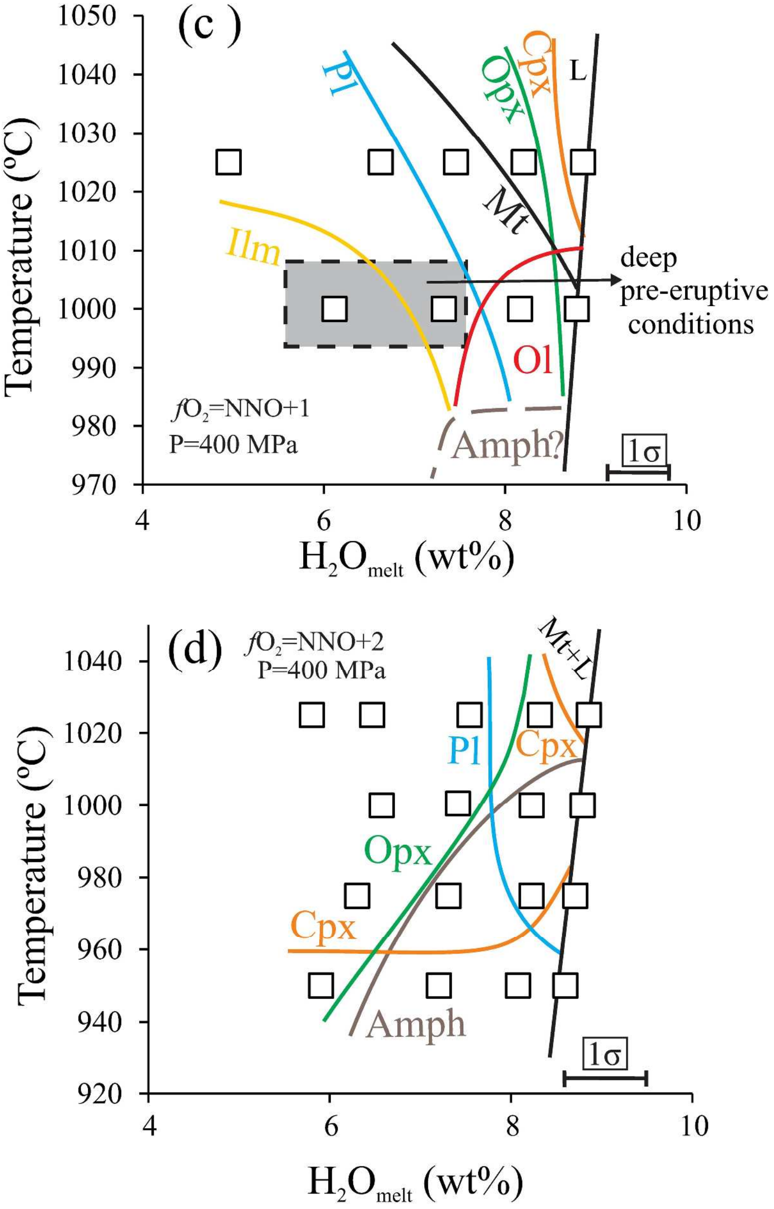

250x391mm (300 x 300 DPI)

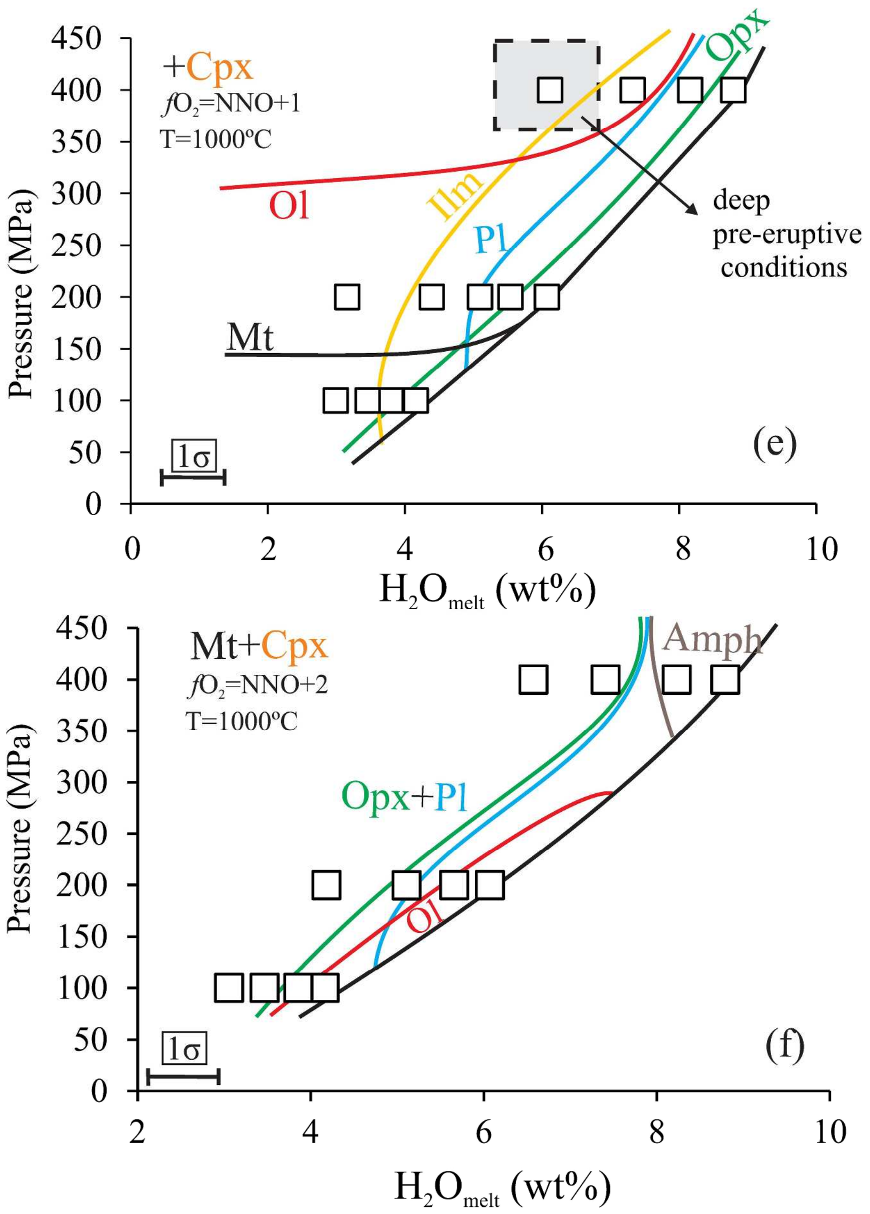

248x347mm (300 x 300 DPI)

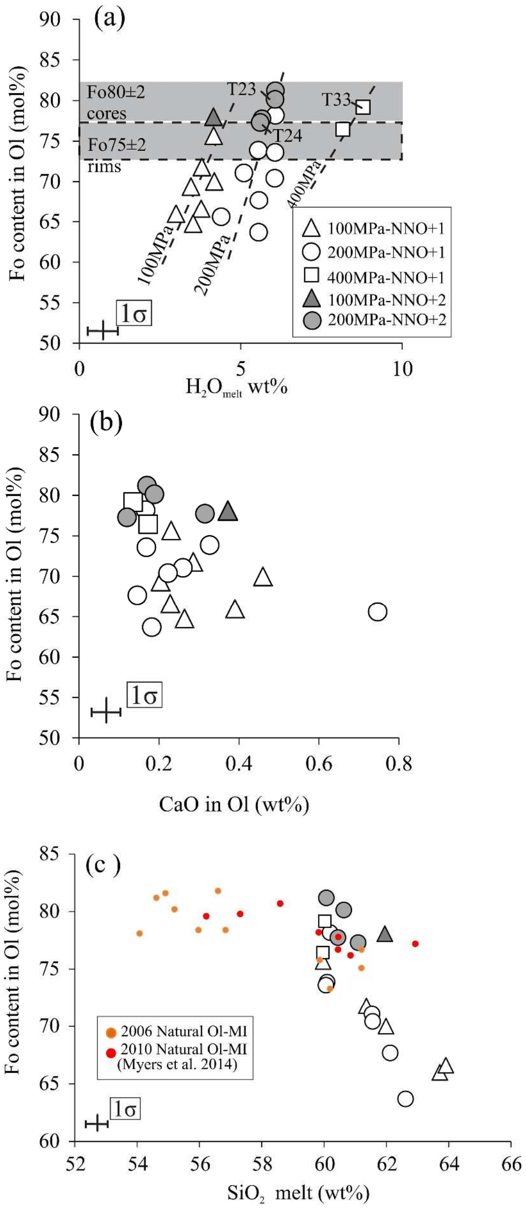

484x1121mm (300 x 300 DPI)

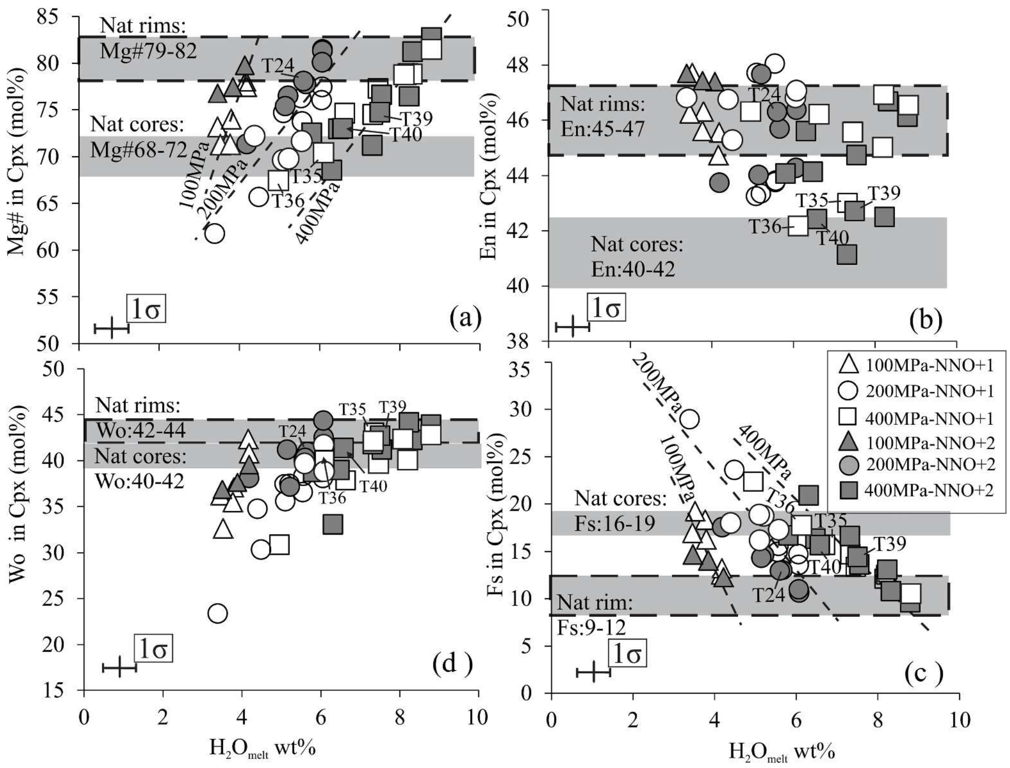

280x212mm (300 x 300 DPI)

T35

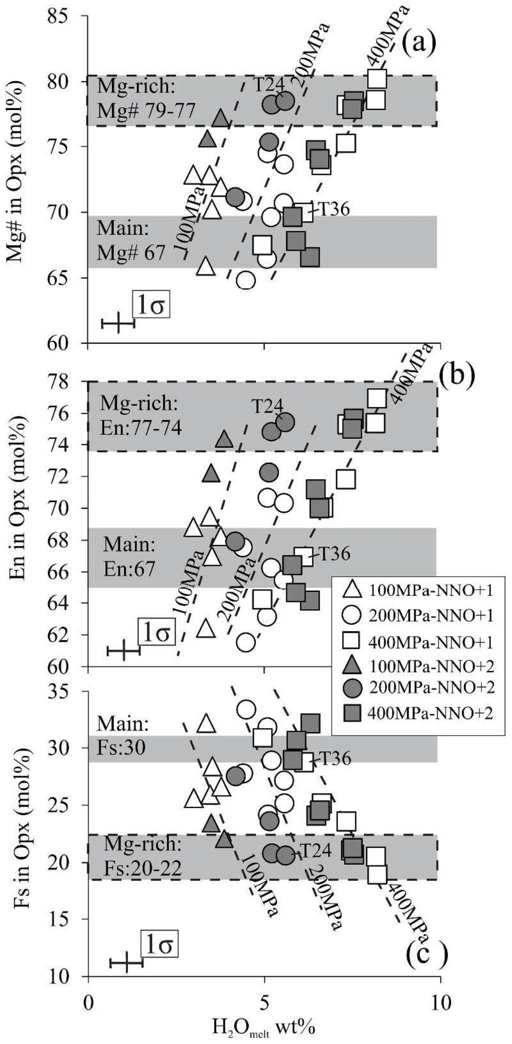

455x765mm (300 x 300 DPI)

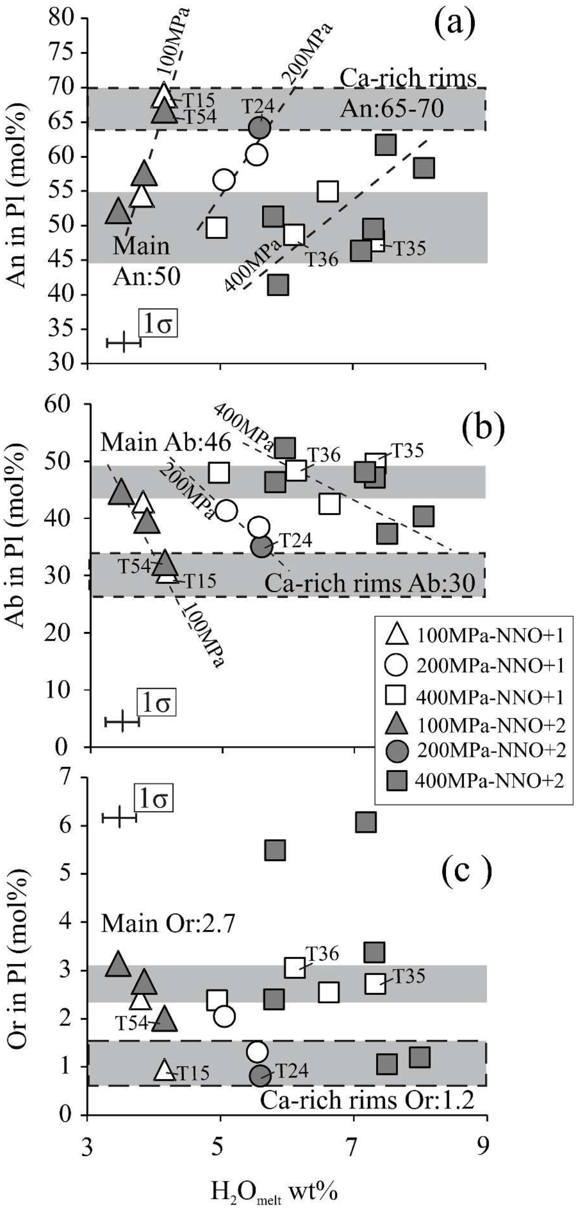

438x920mm (300 x 300 DPI)

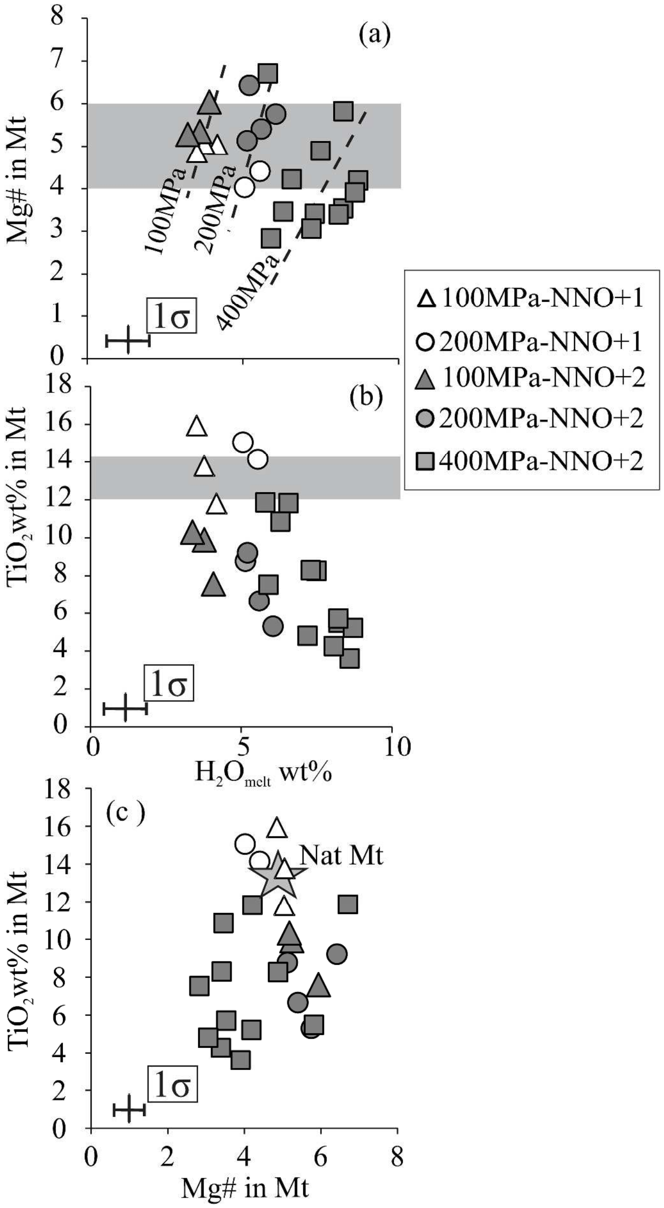

343x626mm (300 x 300 DPI)

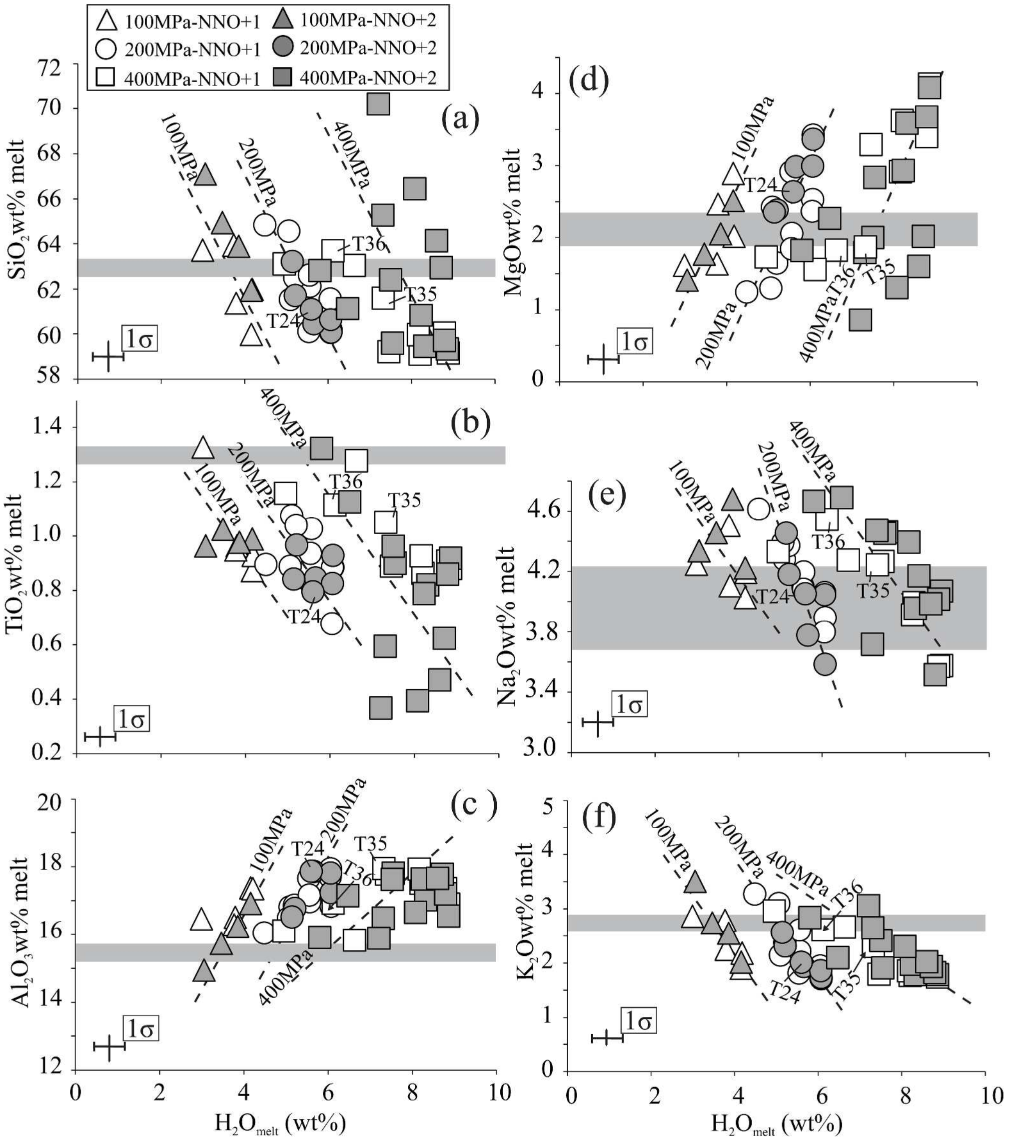

450x509mm (300 x 300 DPI)

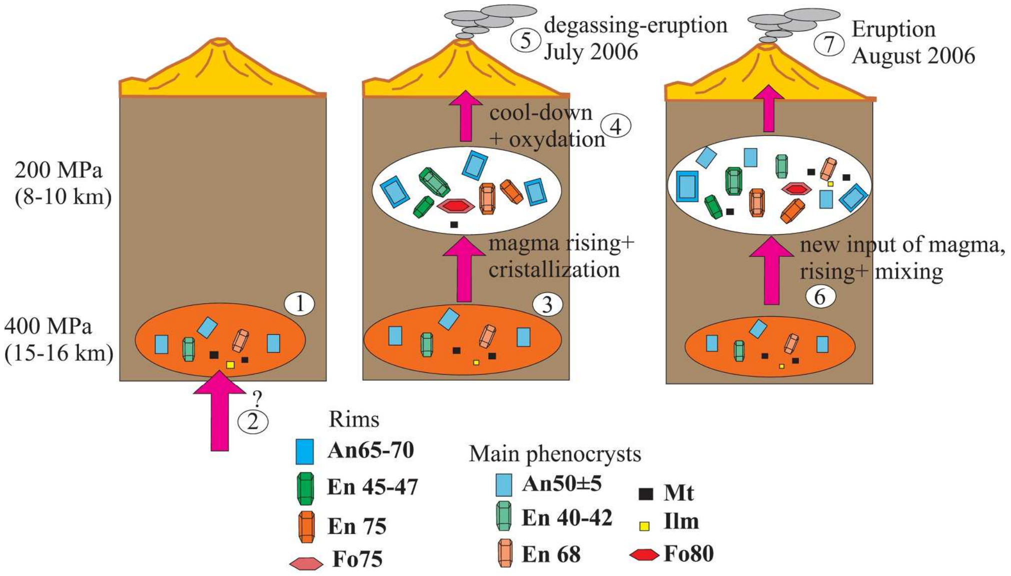

199x114mm (300 x 300 DPI)

Table 1: Representative compositions of the natural sample (bulk-rock and phenocrysts) and starting material

	Bulk rock	Starting material		Pl		Cpx		Opx		Mt		glass	
n		10	sd	20	sd	15	sd	17	sd	10		10	sd
SiO_2	58.00	58.51	0.34	55.29	1.11	50.55	1.22	52.90	1.56	0.13	0.05	62.83	0.41
TiO_2	0.88	0.89	0.10	0.06	0.05	0.62	0.11	0.27	0.10	12.90	0.28	1.27	0.12
Al_2O_3	16.60	16.74	0.16	27.22	0.70	2.17	0.30	1.27	0.15	4.09	0.42	15.54	0.20
FeO*	6.74	6.84	0.32	0.57	0.11	10.99	0.91	18.87	0.69	78.73	0.83	6.23	0.43
MnO	0.12	0.15	0.10	0.03	0.04	0.28	0.09	0.49	0.14	0.34	0.06	0.05	0.04
MgO	4.45	4.18	0.08	0.06	0.02	14.28	0.45	23.96	0.85	3.78	0.52	2.25	0.16
CaO	6.80	7.20	0.07	10.35	0.70	19.90	0.45	1.57	0.16	0.02	0.02	4.81	0.27
Na_2O	3.90	3.53	0.06	5.15	0.42	0.44	0.04	0.04	0.03	0.01	0.01	4.00	0.27
K_2O	1.71	1.76	0.07	0.45	0.09	0.01	0.02	0.01	0.01	0.01	0.01	2.74	0.18
P_2O_5	0.24	0.21	0.10									0.28	0.07
Sum	99.44	100.0		99.17	1.05	99.25	1.44	99.38	1.12	100.00	0.79	96.95	1.10
(ppm)													
Sr	570												
La	18												
Y	17												

Yb	1.48									
La/Yb	12									
Mineral end-members										
An		51.26	3.57							
Ab		46.08	3.31							
Or		2.67	0.53							
En				41.19	1.11	67.41	1.11		0.31	
Fs				17.55	1.38	29.41	0.89		2.77	
Wo				41.25	0.99	3.18	0.35			
Mg#	39.77			69.86	2.14	69.33	1.05	4.6		
										Σr^2
phase proportions (wt%)		28.00		7.10		7.50		1.10	56.00	0.10

Bulk-rock composition and traces from Samaniego *et al*. (2011)

En. Fs. Wo: calculated as in Morimoto (1989)

An= 100[Ca/(Ca+Na+K)]; Ab= 100[Na/(Ca+Na+K)]; Or=[100K/(Ca+Na+K)]. End members calculated as in Deer *et al.* (1972).

Mg# of Cpx, OPx= Mg# = 100[Mg/(Mg+Fe*)]

Mg# of Mt=100*(MgO/FeO*+MgO)

Table 2: experimental conditions and phase proportions (wt%)

NNO+1 experiments

Run	XH_2O_{in}	H_2O_{bdf} (wt%)	H_2O_{calc} (wt%)	fH_2O (bar)	$\log fO_2$ (bar)	ΔNNO		Ol	Cpx	Opx	Pl	Mt	Ilm	Amph	% Crystal	Σr^2
1000ºC/100MPa.97.5 h:			**4.16**	**940**	**-9.7**	**0.63**	**fH_2: 3.47 bar**									
T15	1.00	5.45	4.16	967	-9.7	0.64		2.80	5.00		4.32				12.12	0.20
T16	0.83	6.34	3.80	801	-9.8	0.48		4.10	6.70	trace	16.40				27.20	0.33
T17	0.68		3.46	660	-10.0	0.31		X	X	X	X		X			
T18	0.51	3.99	2.99	490	-10.3	0.05		X	X	X	X					
975ºC/100MPa.94.5h :			**4.18**	**931**	**-10.1**	**0.62**	**fH_2 :3.56 bar**									
T19	1.00	7.08	4.18	977	-10.1	0.61		3.20	9.60		13.11	1.25			27.16	0.15
T20	0.81	6.96	3.77	790	-10.3	0.43		X	X	X	X	X	X			
T21	0.70		3.52	686	-10.4	0.31		X	X	X	X	X	X			
T22	0.63		3.35	617	-10.5	0.21			X	X	X	X	X			
1000ºC/200MPa.77.5 h :			**6.07**	**1864**	**-9.4**	**0.89**	**fH_2 :5.79 bar**									
T10	1.00	7.55	6.07	2107	-9.4	0.86		0.60	3.10			1.44			5.14	0.80
T11	0.83	5.36	5.54	1745	-9.6	0.69		0.30	7.80			1.08			9.18	0.32
T12	0.70	5.76	5.10	1469	-9.8	0.54		0.50	6.80	4.03	12.60	1.10			25.03	0.08

T13	0.51		4.39	1082	-10.0	0.28		X	X	X	X	X				
T14	0.26		3.16	548	-10.6	-0.31		X	X	X	X	X	X			
975ºC/200MPa. 117h:			**6.06**	**1833**	**-9.5**	**1.25**	**$f\mathrm{H}_2$: 3.65 bar**									
T1	1.00	6.94	6.06	2100	-9.5	1.22		1.20	7.80			0.67			9.67	0.30
T2	0.84	6.41	5.56	1760	-9.6	1.06		2.90	8.30	1.50	13.12	0.70			26.52	0.04
T3	0.73	6.22	5.20	1532	-9.7	0.94			8.60	7.40	17.06	0.67			33.73	0.07
T4	0.54	5.56	4.48	1128	-10.0	0.68			X	X	X	X	X			
T5	0.30		3.38	632	-10.5	0.17			X	X	X	X	X			
950ºC/200MPa. 95 h:			**6.05**	**1812**	**-10.1**	**1.02**	**$f\mathrm{H}_2$: 4.54 bar**									
T6	1.00	7.62	6.05	2093	-10.1	0.99		0.90	1.30			0.60		14.90	17.70	0.38
T7	0.84	6.35	5.55	1754	-10.2	0.84		1.80	10.30	2.71	18.36	0.98		1.10	35.25	0.02
T8	0.69	5.54	5.06	1447	-10.4	0.67			4.90	13.90	31.06	0.21	1.40		51.47	0.70
T9	0.49		4.28	1026	-10.7	0.37			X	X	X		X			
1025ºC/400 MPa. 92 h :8.86				**4129**	**-9.7**	**0.26**	**$f\mathrm{H}_2$: 26.92 bar**									
T28	1.00	12.31	8.86	4596	-9.7	0.19									0.00	
T29	0.85	8.12	8.20	3922	-9.8	0.06			5.40	0.20					5.60	0.34
T30	0.70	7.49	7.46	3221	-10.0	-0.11			7.10	1.10					8.20	0.55
T31	0.55	5.45	6.63	2525	-10.2	-0.33			8.10	6.50	25.60	1.20			41.40	0.26
T32	0.30	4.90	4.95	1383	-10.7	-0.85			12.80	4.80	26.80	0.87			45.27	0.29
1000ºC/400MPa. 69.5 h: 8.79				**4079**	**-9.5**	**0.85**	**$f\mathrm{H}_2$: 12.96 bar**									

T33	1.00	9.88	8.79	4521	-9.5	0.78		0.10	4.90			1.30			6.30	0.31
T34	0.86	7.32	8.16	3881	-9.6	0.65		0.30	8.80	trace		0.78			9.88	0.11
T35	0.69	5.53	7.32	3103	-9.8	0.45			11.20	4.80	11.90	1.33			29.23	0.16
T36	0.47	4.89	6.12	2142	-10.1	0.13			13.00	6.50	24.85	1.38	traces		45.73	0.16

NNO+2 experiments

1000ºC/100MPa. 70 h :			**4.16**	**940**	**-8.8**	**1.53**	***f*$\mathbf{H_2}$: 1.24 bar**									
T54	1.00	5.31	4.16	967	-8.8	1.51		2.60	6.40		12.90	1.99			23.89	0.07
T55	0.86	4.92	3.86	827	-8.9	1.40			8.40	5.00	25.50	2.70			41.60	0.18
T56	0.69	4.36	3.47	664	-9.1	1.21			8.00	6.10	33.30	3.00			50.40	0.24
T57	0.53	3.10	3.06	512	-9.3	0.98			X	X	X	X				
1000ºC/200MPa. 101 h :			**6.07**	**1864**	**-8.5**	**1.84**	***f*$\mathbf{H_2}$: 1.94 bar**									
T45b	1.00	7.52	6.07	2107	-8.5	1.81		0.40	4.60			1.20			6.20	0.38
T46b	0.86	6.64	5.66	1823	-8.6	1.68		0.20	8.20			1.42			9.82	0.14
T47b	0.73	6.06	5.21	1539	-8.8	1.53			7.50	3.70	12.60	1.51			25.31	0.02
T48b	0.46		4.18	978	-9.2	1.14			X	X	X	X				
975ºC/200MPa. 117h :			**6.06**	**1833**	**-8.9**	**1.84**	***f*$\mathbf{H_2}$: 1.85 bar**									
T23	1.00	7.88	6.06	2100	-8.9	1.81		0.40	7.40			1.90			9.70	0.18

T24	0.85	6.60	5.60	1783	-9.0	1.66		0.20	9.60	0.88	5.20	1.60			17.48	0.01
T25	0.71	6.17	5.14	1497	-9.2	1.51			9.40	3.60	16.30	2.40			31.70	0.14
T26	0.51		4.39	1078	-9.4	1.23			X	X	X	X				
T27	0.36		3.68	751	-9.5	1.12										
1025ºC/400MPa. 97.5 h:			**8.86**	**4129**	**-8.2**	**1.77**	***f*H_2 : 4.77 bar**									
T49	1.00	10.40	8.86	4596	-8.2	1.70						1.30			1.30	0.47
T50	0.88	6.99	8.32	4034	-8.3	1.58			4.30			0.90			5.20	0.46
T51	0.72	5.12	7.55	3300	-8.5	1.41			7.90	1.30		0.60			9.80	0.38
T52	0.52	4.57	6.47	2403	-8.8	1.13			9.70	4.22	13.83	1.30			29.05	0.52
T53	0.42	4.13	5.80	1921	-9.0	0.94			8.10	8.50	27.00	1.40			44.9	0.46
1000ºC/400MPa. 91 h :			**8.79**	**4079**	**-8.4**	**1.88**	***f*H_2 : 3.94 bar**									
T37	1.00	9.72	8.79	4521	-8.4	1.82			4.70			1.20		traces	5.90	0.3
T38	0.87	7.80	8.23	3947	-8.6	1.70			6.40			1.40		4.20	12.00	0.15
T39	0.72	6.50	7.50	3259	-8.7	1.53			10.60	4.10	13.00	2.60			30.30	0.10
T40	0.55		6.57	2485	-9.0	1.29			X	X	X	X				
975ºC/400MPa. 92h :			**8.71**	**4004**	**-8.9**	**1.80**	***f*H_2 :4.10 bar**									
T41	1.00	10.09	8.71	4437	-8.9	1.73						X		X		
T42	0.89		8.23	3943	-9.0	1.63			X			X		X		
T43	0.70	6.15	7.31	3093	-9.2	1.41			7.80		18.60	2.60		12.20	41.20	0.29
T44	0.51		6.30	2277	-9.5	1.15			X	X	X	X	X			

950ºC/400MPa.93.5h :			**8.60**	**3948**	**-8.8**	**2.27**	**fH_2 : 2.23 bar**									
T45	1.00	9.28	8.60	4322	-8.8	2.20						1.80		20.50	22.30	0.51
T46	0.88	7.40	8.08	3797	-8.9	2.09					10.80	2.10		22.50	35.40	0.33
T47	0.69	5.53	7.21	3001	-9.2	1.88					21.11	2.90		24.60	48.61	0.38
T48	0.46		5.91	1991	-9.5	1.53				X	X	X		X		

XH_2O_{in}:initial H2O/(H2O+CO2) in the charge (in moles)

H_2O_{calc}: water content in the melt a:determined by the solubility model of Papale *et al.* (2006) and using the methodlogy of Scaillet & Macdonald (2006)
H_2O_{bdf}:determined by difference method (see text for details)

fH_2(bar):hydrogen fugacity of the experiment. determined by using NiPd alloy sensors. (see text for details)

log fO_2(bar): logarithm of the oxygen fugacity calculated from the experimental fH_2

ΔNNO:log fO_2-log fO_2 of the NNO buffer calculated at P and T (NNO: Pownceby & O'Neill.1994)

X: mineral phase identified by SEM but. its abundance could not be calculated

% Crystal : numbers indicate the phase abundance in the charge in weight %

Gl:glass. Ol: olivine. Cpx:clinopyroxene. Mt:magnetite.Pl:plagioclase.Opx:orthopyroxene. Ilm:ilmenite.Amph:amphibole

Trace: phase with a modal abundance < 0.1 wt%

Table 3: experimental olivines

NNO+1 experiments

	n													
1000ºC/100MPa		SiO_2	TiO_2	Al_2O_3	MgO	CaO	MnO	FeO*	Na_2O	K_2O	Sum	Fo	Kd^{Fe*-Mg}	$KdFe^{2+}$
T15	3	38.61	0.00	0.05	38.89	0.23	0.36	22.30	0.01	0.00	100.44	75.66	0.26	0.37
sd		0.40	0.00	0.01	0.20	0.05	0.14	0.61	0.01	0.00	0.47	0.60		
T16	3	38.71	0.07	0.22	35.41	0.29	0.34	24.79	0.02	0.04	99.88	71.80	0.28	0.38
sd		0.39	0.05	0.09	0.76	0.04	0.04	0.37	0.03	0.04	0.81	0.38		
T17	2	37.84	0.00	0.09	34.40	0.20	0.34	27.07	0.02	0.02	99.97	69.37		
sd		0.20	0.00	0.04	0.30	0.03	0.00	0.02	0.01	0.03	0.11	0.20		
T18	1	37.23	0.10	0.10	31.72	0.39	0.43	29.14	0.01	0.05	99.18	65.99	0.30	0.39
975ºC/100MPa														
T19	2	37.39	0.02	0.38	33.40	0.46	0.33	25.51	0.06	0.04	97.58	70.01	0.27	0.38
sd		0.46	0.02	0.49	0.56	0.37	0.10	0.36	0.05	0.05	0.26	0.05		
T20	2	37.97	0.00	0.04	31.73	0.23	0.51	28.34	0.00	0.01	98.81	66.62	0.28	0.38
sd		0.25	0.00	0.04	0.38	0.00	0.01	0.37	0.00	0.01	0.20	0.56		
T21	2	37.14	0.01	0.03	31.34	0.26	0.46	30.39	0.03	0.04	99.69	64.76		
sd		0.12	0.01	0.03	0.33	0.02	0.03	0.03	0.00	0.03	0.27	0.22		

T22															
1000ºC/200MPa															
T10	3	38.72	0.01	0.03	40.72	0.17	0.38	20.26	0.01	0.02	100.31	78.18	0.28		0.40
sd		0.13	0.02	0.03	0.86	0.06	0.10	0.47	0.01	0.02	0.84	0.53			
T11	4	39.29	0.01	0.18	36.92	0.33	0.36	23.26	0.02	0.01	100.37	73.87	0.31		0.43
sd		1.42	0.01	0.17	1.48	0.18	0.06	0.66	0.01	0.01	0.64	0.71			
T12	4	37.92	0.05	0.04	35.75	0.26	0.35	25.95	0.01	0.02	100.35	71.06	0.30		0.41
sd		0.58	0.05	0.03	0.72	0.07	0.14	0.75	0.01	0.02	0.88	0.46			
T13	3	37.17	0.05	0.14	31.52	0.75	0.37	29.45	0.03	0.00	99.48	65.61			
sd		0.34	0.07	0.13	0.76	0.51	0.04	1.14	0.03	0.01	1.22	0.49			
975ºC/200MPa															
T1	3	38.32	0.08	0.06	37.78	0.17	0.34	24.14	0.01	0.00	100.89	73.61	0.26		0.40
sd		0.17	0.07	0.04	0.47	0.02	0.08	0.38	0.01	0.00	0.17	0.53			
T2	2	36.94	0.01	0.00	33.61	0.15	0.50	28.60	0.00	0.04	99.85	67.68	0.30		0.44
sd		0.05	0.01	0.00	0.11	0.05	0.06	0.14	0.00	0.03	0.27	0.03			
950ºC/200MPa															
T6	2	37.62	0.00	0.12	34.63	0.22	0.30	25.93	0.01	0.04	98.88	70.42			
		0.02	0.00	0.17	0.40	0.17	0.02	0.17	0.01	0.02	0.84	0.10			
T7	1	36.52	0.00	0.00	30.54	0.18	0.35	31.03	0.01	0.02	98.65	63.69			
1000ºC/400MPa															

T33	4	39.00	0.03	0.01	40.85	0.14	0.25	19.16	0.00	0.02	99.46	79.17	0.26		0.37
sd		0.44	0.05	0.01	0.27	0.01	0.02	0.42	0.00	0.02	0.46	0.41			
T34	3	38.91	0.04	0.02	39.02	0.17	0.28	21.43	0.01	0.00	99.87	76.44	0.25		0.35
sd		0.44	0.05	0.02	0.91	0.03	0.01	0.16	0.01	0.00	1.53	0.28			

NNO+2 experiments

1000ºC/100MPa

T54	3	39.84	0.01	0.36	39.40	0.37	0.28	19.71	0.03	0.01	100.02	78.08			
		0.21	0.02	0.38	0.68	0.21	0.10	0.15	0.03	0.02	0.18	0.29			

1000ºC/200MPa

T45b	3	39.67	0.01	0.02	42.45	0.17	0.20	17.52	0.01	0.02	100.07	81.20	0.22		0.37
sd		0.90	0.01	0.01	0.95	0.02	0.14	0.58	0.01	0.04	0.58	0.66			
T46b	3	39.25	0.01	0.06	40.19	0.32	0.23	20.50	0.02	0.00	100.57	77.74	0.26		0.43
sd		0.87	0.02	0.05	0.76	0.33	0.06	0.33	0.02	0.01	0.22	0.19			

975ºC/200MPa

T23	2	38.82	0.00	0.01	42.93	0.19	0.44	18.97	0.02	0.02	101.40	80.14	0.24		0.42
sd		0.35	0.00	0.01	0.36	0.04	0.15	0.00	0.01	0.00	0.21	0.14			
T24	1	38.86	0.00	0.00	40.74	0.12	0.31	21.33	0.02	0.00	101.37	77.30	0.25		0.40

n: number of analysis

sd: standard deviation

FeO*: Total iron reported as Fe2+

Fo mol(%)=100 Mg/(Mg+ Fe*) in olivine

KdFe*-Mg =(Fe/Mg in ol)/(Fe/Mg in melt).

KdFe2+=Fe/Mg in ol)/(Fe2+/Mg in melt) after Kress & Carmichael (1991).

Table 4. Composition of experimental clinopyroxenes (wt%)

NNO+1 experiments

1000ºC/100MPa	n	SiO_2	TiO_2	Al_2O_3	MgO	CaO	MnO	FeO*	Na_2O	K_2O	Sum	En	Fs	Wo	Mg#	KdFe*-Mg
T15	2	52.06	0.83	3.98	15.44	20.33	0.22	7.72	0.35	0.06	100.99	44.74	12.55	42.34	78.09	0.23
sd		0.17	0.08	0.66	0.27	0.04	0.05	0.12	0.07	0.00	0.47	0.52	0.27	0.33	0.57	
T16	3	50.74	0.81	3.47	16.28	18.12	0.21	10.20	0.29	0.02	100.14	46.31	16.28	37.07	74.00	0.25
sd		0.46	0.15	0.09	0.50	0.56	0.03	0.67	0.00	0.02	0.27	0.78	0.84	1.66	0.67	
T17	2	51.27	0.57	2.77	15.91	17.33	0.36	10.40	0.25	0.06	98.92	46.24	16.96	36.20	73.16	
sd		0.66	0.09	0.64	0.60	0.17	0.05	0.16	0.08	0.02	0.65	0.86	0.59	0.33	1.04	
975ºC/100MPa																
T19	2	51.25	0.74	3.92	15.34	19.12	0.25	7.94	0.37	0.11	99.04	45.55	13.22	40.81	77.50	0.19
sd		0.31	0.04	0.42	0.35	0.05	0.05	0.28	0.07	0.04	0.36	0.44	0.29	0.63	0.22	
T20	1	50.45	0.94	2.75	15.88	17.17	0.37	11.38	0.30	0.06	99.29	45.61	18.33	35.46	71.33	0.22
T21	2	51.72	0.89	2.67	16.36	15.57	0.26	11.75	0.23	0.16	99.60	47.71	19.22	32.63	71.28	
sd		0.54	0.33	0.07	0.01	0.60	0.14	0.02	0.01	0.11	0.34	0.74	0.25	0.76	0.05	
1000ºC/200MPa																
T10	5	52.10	0.51	2.57	16.52	20.39	0.23	6.69	0.27	0.04	99.32	47.11	10.71	41.81	81.48	0.23
sd		0.53	0.16	0.46	0.29	0.26	0.15	0.07	0.06	0.04	0.18	0.50	0.18	0.52	0.38	

T11	2	51.44	0.76	3.57	16.72	17.70	0.26	9.29	0.25	0.05	100.01	48.06	14.97	36.56	76.26	0.27
sd		0.04	0.08	0.28	0.31	0.30	0.09	1.01	0.03	0.00	0.68	1.02	1.59	0.72	2.31	
T12	5	51.33	0.67	3.52	16.34	16.94	0.32	9.88	0.38	0.06	99.43	47.72	16.18	35.57	74.68	0.25
sd		0.15	0.05	0.91	0.66	0.35	0.09	0.46	0.10	0.02	0.34	0.86	0.34	1.05	0.27	
T13	1	51.15	0.79	2.96	15.74	16.28	0.30	10.79	0.25	0.05	98.31	46.75	17.98	34.76	72.22	
975ºC/200MPa																
T1	3	51.91	0.41	1.89	16.59	19.21	0.33	8.59	0.17	0.02	99.12	46.85	13.61	39.01	77.49	0.21
sd		0.58	0.11	0.57	0.50	0.24	0.03	0.35	0.08	0.03	0.44	0.70	0.34	1.09	0.18	
T2	4	50.06	0.85	4.02	14.92	18.97	0.30	9.47	0.33	0.04	98.96	43.82	15.60	40.08	73.74	0.22
sd		0.21	0.18	0.03	0.37	0.21	0.12	0.22	0.03	0.05	0.14	0.85	0.34	0.68	0.63	
T3	2	49.74	0.89	3.41	14.65	17.63	0.26	11.29	0.32	0.04	98.23	43.35	18.73	37.49	69.82	0.22
sd		0.10	0.01	0.15	0.22	0.59	0.10	0.44	0.05	0.01	0.78	1.16	0.51	0.82	1.14	
T4	1	50.94	0.67	2.60	15.19	14.17	0.45	14.13	0.32	0.10	98.56	45.26	23.62	30.35	65.71	0.24
T5	1	51.20	0.62	3.06	15.52	10.78	0.49	17.11	0.57	0.10	99.44	46.81	28.96	23.38	61.78	
950ºC/200MPa																
T6	1	52.50	0.29	1.72	16.04	18.16	0.24	9.01	0.23	0.00	98.17	46.78	14.74	38.07	76.04	0.23
T7	1	50.28	1.05	3.46	14.51	17.66	0.36	10.22	0.35	0.13	98.00	43.78	17.30	38.31	71.67	0.22
T8	2	51.00	0.68	2.83	14.69	17.66	0.24	11.44	0.33	0.12	98.98	43.26	18.89	37.44	69.60	0.20
sd		0.67	0.23	0.84	0.95	0.53	0.09	0.79	0.07	0.11	0.53	1.59	0.76	2.18	0.08	
1025ºC/400 MPa																

T29	1	51.21	0.77	3.53	16.27	19.36	0.24	7.75	0.35	0.06	99.55	46.92	12.54	40.14	78.91	0.27
T30	3	51.83	0.62	4.10	15.48	19.22	0.24	8.10	0.39	0.16	100.13	45.58	13.38	40.64	77.32	0.28
		0.11	0.03	0.71	0.35	1.36	0.08	0.11	0.08	0.14	1.11	0.90	0.38	1.15	0.15	
T31	1	52.38	0.48	2.90	15.65	17.88	0.23	9.49	0.44	0.16	99.59	46.10	15.67	37.85	74.63	0.17
T32	1	50.48	0.92	2.87	15.93	14.78	0.28	13.71	0.35	0.04	99.38	46.30	22.36	30.87	67.43	0.26
1000ºC/400MPa																
T33	3	51.84	0.40	2.23	16.36	20.97	0.07	6.56	0.27	0.01	98.72	46.54	10.47	42.88	81.64	0.22
sd		1.07	0.06	0.82	0.38	0.30	0.05	0.38	0.04	0.01	0.82	0.90	0.62	0.78	1.08	
T34	3	51.14	0.71	3.64	15.50	20.28	0.29	7.44	0.41	0.04	99.44	45.03	12.12	42.36	78.79	0.22
sd		0.75	0.10	0.32	0.26	0.10	0.09	0.16	0.08	0.01	0.35	0.55	0.31	0.39	0.63	
T35	1	49.27	0.78	4.56	14.30	19.51	0.04	8.72	0.36	0.06	97.60	43.01	14.72	42.19	74.50	0.21
T36	2	50.63	0.93	5.25	13.63	17.83	0.24	10.23	0.57	0.15	99.47	42.17	17.76	39.64	70.38	0.20
sd		0.30	0.04	0.67	0.01	0.82	0.14	0.33	0.13	0.07	0.88	0.44	0.75	1.44	0.66	

NNO+2 experiments

1000ºC/100MPa

T54	2	52.27	0.59	2.91	16.54	19.42	0.26	7.68	0.28	0.02	99.96	47.32	12.32	39.94	79.35	0.22
sd		0.49	0.19	0.15	0.26	0.62	0.00	0.45	0.02	0.02	0.19	0.66	0.70	1.35	0.70	

T55	2	52.25	0.76	2.82	16.42	18.31	0.31	8.77	0.31	0.05	99.99	47.35	14.19	37.96	76.95	0.23
sd		0.36	0.28	0.65	0.33	0.51	0.05	0.06	0.01	0.07	0.34	0.00	0.39	0.32	0.48	
T56	3	52.32	0.71	2.35	16.55	17.97	0.25	9.18	0.27	0.05	99.65	47.61	14.83	37.16	76.26	0.21
sd		0.01	0.03	0.01	0.16	0.33	0.05	0.02	0.04	0.04	0.49	0.10	0.21	0.25	0.22	
1000ºC/200MPa																
T45b	2	50.52	0.56	3.02	15.69	20.02	0.27	6.42	0.27	0.09	96.88	46.37	10.64	42.53	81.34	0.22
sd		0.57	0.16	0.02	0.13	0.10	0.05	0.47	0.02	0.00	0.09	0.09	0.66	0.66	0.98	
T46b	1	50.44	0.77	4.53	15.77	19.66	0.19	8.02	0.38	0.09	99.84	45.70	13.04	40.95	77.80	0.26
T47b	4	50.85	0.80	3.50	16.80	18.22	0.34	9.19	0.30	0.04	100.05	47.67	14.63	37.15	76.53	0.22
sd		0.35	0.08	0.47	0.22	0.62	0.08	0.47	0.05	0.04	0.84	0.55	0.75	1.27	0.80	
T48b	1	52.23	0.99	3.29	15.02	18.19	0.37	10.75	0.31	0.16	101.31	43.75	17.56	38.09	71.36	
975ºC/200MPa																
T23	1	50.91	0.68	3.38	15.65	21.80	0.23	6.92	0.29	0.05	99.90	44.28	10.99	44.35	80.12	0.24
sd																
T24	1	50.06	0.65	3.86	16.53	20.03	0.26	8.26	0.36	0.05	100.05	46.30	12.98	40.31	78.11	0.23
T25	1	50.17	0.87	4.28	15.17	19.76	0.25	8.82	0.46	0.04	99.82	44.03	14.35	41.21	75.42	0.27
1025ºC/400MPa																
T50	5	51.34	0.58	3.58	15.91	20.04	0.16	6.55	0.39	0.10	98.65	46.68	10.80	42.26	81.24	0.24
sd		0.87	0.19	0.69	0.55	0.71	0.09	0.80	0.06	0.07	0.33	0.67	1.50	0.78	2.32	
T51	2	50.13	0.75	4.81	15.21	19.50	0.23	8.28	0.42	0.04	99.38	44.74	13.66	41.22	76.61	0.26

sd		0.00	0.06	0.41	0.20	0.38	0.32	0.16	0.01	0.05	0.86	0.81	0.33	0.61	0.11	
T52	3	51.48	0.81	4.75	14.68	18.04	0.29	9.69	0.50	0.16	100.40	44.14	16.35	39.00	72.97	0.26
sd		0.46	0.17	0.62	0.33	0.29	0.00	0.37	0.03	0.04	0.58	0.12	0.28	0.24	0.37	
T53		51.51	0.83	3.46	14.56	17.80	0.29	9.83	0.48	0.10	98.87	44.08	16.69	38.72	72.53	0.21
1000^{a}C/400MPa																
T37	2	51.89	0.55	2.67	16.13	21.37	0.21	5.99	0.35	0.05	99.21	46.12	9.62	43.93	82.74	0.22
sd		0.75	0.27	0.35	0.49	0.13	0.11	0.20	0.02	0.02	0.42	0.86	0.43	0.25	0.90	
T38	2	49.80	0.85	5.29	14.14	20.45	0.15	7.76	0.43	0.10	98.97	42.50	13.09	44.16	76.45	0.29
sd		0.18	0.05	0.59	0.15	0.56	0.04	0.06	0.07	0.07	0.23	0.28	0.12	0.47	0.05	
T39	3	49.77	0.90	5.24	14.15	19.70	0.07	8.53	0.52	0.09	98.99	42.72	14.44	42.72	74.74	0.25
sd		0.71	0.09	0.44	0.36	0.89	0.06	0.48	0.13	0.10	0.87	0.61	0.29	0.30	0.64	
T40	1	50.48	0.80	4.62	13.91	18.87	0.29	9.16	0.54	0.02	98.70	42.43	15.68	41.39	73.01	
975^{a}C/400MPa																
T43	1	51.93	0.60	4.49	13.66	19.31	0.25	9.84	0.53	0.09	100.69	41.14	16.63	41.80	71.21	0.32
T44	1	50.67	0.65	3.62	15.34	15.47	0.25	12.53	0.46	0.10	99.09	45.61	20.90	33.06	68.58	

n: number of analyses; sd: standard deviation; FeO*: Total Iron reported as FeO

En. Fs. Wo: calculated as in Morimoto (1989); Mg# = 100[Mg/(Mg+Fe*)]

KdFe*-Mg= (Fe*/Mg in clinopyroxene)/(Fe*/Mg in melt)

Table 5: Composition of experimental orthopyroxenes (wt%).

NNO+1 experiments

	n															
1000ºC/100MPa		SiO_2	TiO_2	Al_2O_3	MgO	CaO	MnO	FeO*	Na_2O	K_2O	Total	En	Fs	Wo	Mg#	Kd^{Fe*-Mg}
T17	1	53.40	0.47	1.77	24.89	1.97	0.40	16.55	0.08	0.06	99.58	69.49	25.92	3.95	72.83	
T18	1	54.00	0.60	1.54	24.62	2.50	0.33	16.33	0.04	0.00	99.96	68.83	25.62	5.03	72.87	0.22
975ºC/100MPa																
T19																
T20	3	53.79	0.45	1.89	23.71	2.19	0.37	16.49	0.08	0.02	98.97	68.24	26.62	4.53	71.93	0.22
sd		1.33	0.24	0.35	0.38	0.34	0.14	0.20	0.06	0.01	0.65	0.60	0.12	0.74	0.09	
T21	2	52.95	0.52	1.66	23.44	2.06	0.24	17.70	0.03	0.00	98.60	67.00	28.39	4.23	70.23	
sd		0.65	0.15	0.31	0.27	0.56	0.09	0.06	0.00	0.00	0.63	0.87	0.13	1.15	0.18	
T22	1	52.57	0.42	1.28	22.76	2.36	0.42	20.95	0.06	0.05	100.87	62.44	32.25	4.66	65.94	
1000ºC/200MPa																
T12	4	53.56	0.30	2.49	25.51	2.27	0.39	15.56	0.07	0.03	100.17	70.66	24.19	4.53	74.50	0.25
sd		0.55	0.12	1.05	0.68	0.22	0.11	0.11	0.07	0.02	0.12	0.81	0.39	0.50	0.52	
T13	3	53.24	0.38	1.70	24.23	1.95	0.49	17.76	0.02	0.02	99.79	67.55	27.78	3.90	70.86	
sd		0.35	0.08	0.66	0.50	0.17	0.08	0.29	0.01	0.03	0.41	0.07	0.42	0.28	0.51	
975ºC/200MPa																

T1																
T2	1	52.42	0.37	3.59	25.58	2.02	0.33	16.31	0.09	0.02	100.72	70.33	25.16	3.99	73.65	0.22
T3	4	51.60	0.45	2.43	23.06	2.09	0.32	17.94	0.03	0.02	97.93	66.26	28.90	4.31	69.63	0.22
sd		0.26	0.12	0.24	0.09	0.09	0.09	0.40	0.01	0.02	0.45	0.43	0.52	0.20	0.52	
T4	4	51.66	0.33	1.54	21.19	2.07	0.45	20.52	0.04	0.03	97.83	61.53	33.42	4.31	64.81	0.25
sd		0.19	0.07	0.20	0.22	0.23	0.10	0.68	0.03	0.03	0.74	0.39	0.75	0.53	0.59	
T5																
950ºC/200MPa																
T7	1	52.02	0.41	3.01	22.03	3.22	0.28	16.28	0.20	0.07	97.50	65.50	27.16	6.87	70.69	0.23
sd																
T8	4	51.31	0.38	1.98	22.46	2.24	0.28	20.20	0.06	0.03	98.94	63.15	31.87	4.55	66.46	0.23
sd		0.60	0.06	0.70	0.70	0.52	0.11	0.62	0.06	0.03	0.58	0.67	0.45	1.14	0.25	
1025ºC/400 MPa																
T28																
T29	3	54.05	0.22	2.45	28.02	1.84	0.30	12.32	0.03	0.02	99.25	76.94	18.97	3.63	80.22	0.25
sd		0.79	0.08	0.46	0.12	0.25	0.08	0.35	0.02	0.02	0.96	0.27	0.48	0.49	0.43	
T30	3	54.95	0.20	1.94	27.41	1.68	0.19	13.66	0.06	0.04	100.14	75.32	21.07	3.31	78.14	0.27
sd		0.80	0.05	0.98	0.81	0.24	0.05	0.18	0.00	0.00	0.68	0.35	0.80	0.38	0.73	
T31	3	52.10	0.37	3.26	24.94	2.14	0.27	15.95	0.03	0.02	99.08	70.09	25.15	4.32	73.59	0.18
sd		0.57	0.04	0.82	0.20	0.27	0.07	0.30	0.03	0.02	0.35	0.77	0.36	0.53	0.48	

T32	3	52.14	0.55	1.91	22.73	2.11	0.35	19.51	0.08	0.03	99.41	64.23	30.92	4.29	67.50	0.26
sd		0.23	0.11	0.29	0.18	0.21	0.17	0.15	0.03	0.03	0.29	0.58	0.29	0.41	0.33	

1000ºC/400MPa

T34	1	54.10	0.17	1.78	27.60	1.86	0.28	13.40	0.02	0.00	99.21	75.39	20.53	3.65	78.60	0.23
sd																
T35	3	52.84	0.27	3.28	24.31	1.92	0.34	15.53	0.07	0.03	98.58	71.82	23.58	4.09	75.28	0.22
sd		0.53	0.12	0.98	0.84	0.08	0.06	2.11	0.04	0.06	0.59	0.04	0.23	0.09	0.19	
T36	2	51.65	0.46	3.01	23.29	1.78	0.38	17.83	0.04	0.06	98.50	66.94	28.75	3.68	69.96	0.20
sd		0.61	0.06	0.08	0.14	0.08	0.05	0.13	0.02	0.00	0.51	0.33	0.23	0.18	0.28	

NNO+2 experiments

1000ºC/100MPa

T55	3	54.35	0.30	1.87	27.12	1.64	0.25	14.45	0.01	0.03	100.02	74.21	22.18	3.23	76.99	0.23
sd		0.43	0.11	0.32	0.10	0.09	0.16	0.40	0.02	0.04	0.92	0.46	0.50	0.17	0.48	
T56	3	54.08	0.34	1.99	26.02	1.96	0.34	15.16	0.04	0.01	99.95	72.03	23.54	3.90	75.37	0.22
sd		0.35	0.10	0.12	0.14	0.28	0.16	0.67	0.03	0.02	0.49	0.35	0.88	0.59	0.74	

1000ºC/200MPa

T47b	2	54.30	0.42	2.67	27.46	2.05	0.23	13.61	0.06	0.03	100.82	74.83	20.80	4.01	78.25	0.20

sd		0.33	0.09	0.60	0.38	0.20	0.06	0.93	0.00	0.05	0.10	1.11	1.40	0.39	1.40	
T48b	4	53.29	0.45	2.02	24.51	2.03	0.33	17.71	0.05	0.01	100.39	67.92	27.53	4.04	71.15	
sd		0.07	0.06	0.07	0.03	0.21	0.16	0.26	0.06	0.01	0.54	0.71	0.09	0.37	0.28	
975ºC/200MPa																
T24	1	53.58	0.40	3.09	28.00	1.80	0.30	13.64	0.03	0.04	100.86	75.45	20.62	3.48	78.53	0.23
T25	1	53.28	0.41	2.04	27.12	1.87	0.37	15.80	0.03	0.04	100.96	72.25	23.61	3.59	75.37	0.28
1025/400MPa																
T51	3	53.65	0.26	3.15	27.36	1.71	0.14	13.34	0.07	0.00	99.67	75.67	20.71	3.40	78.51	0.23
sd		0.29	0.07	0.13	0.29	0.10	0.09	0.26	0.04	0.00	0.64	0.47	0.42	0.22	0.45	0.24
T52	4	53.47	0.33	2.74	25.09	2.06	0.31	15.13	0.10	0.05	99.29	71.19	24.09	4.21	74.72	0.25
sd		0.73	0.08	1.01	0.19	0.31	0.09	0.35	0.07	0.04	0.47	0.19	0.43	0.64	0.31	
T53	3	52.92	0.47	1.95	22.32	3.79	0.39	17.34	0.08	0.05	99.31	66.43	28.95	4.04	69.65	
sd		0.80	0.21	0.41	2.09	3.13	0.07	1.62	0.09	0.04	0.57	0.23	0.02	0.35	0.06	
1000/400MPa																
T39	2	53.17	0.29	3.40	26.66	1.53	0.38	13.47	0.04	0.07	99.00	75.03	21.27	3.09	77.91	0.21
sd		0.73	0.06	0.56	0.05	0.12	0.10	0.23	0.00	0.04	0.50	0.31	0.24	0.23	0.26	
T40	1	53.75	0.46	3.33	24.76	2.39	0.37	15.47	0.08	0.06	100.68	70.01	24.54	4.86	74.04	
975ºC/400MPa																
T44	1	53.43	0.26	1.61	22.81	1.39	0.53	20.41	0.03	0.05	100.53	64.15	32.20	2.81	66.58	
950/400MPa																

T48	1	50.58	1.62	2.15	23.48	2.07	0.34	19.86	0.07	0.00	100.16	64.68	30.70	4.09	67.81

n: number of analyses

sd: Standard deviation

FeO*: Total Iron reported as FeO

En. Fs. Wo: calculated as in Morimoto (1989)

Mg# = 100[Mg/(Mg+Fe*)]

KdFe*-Mg= (Fe*/Mg in clinopyroxene)/(Fe*/Mg in melt)

Table 6: representative composition of experimental plagioclase.

sample	n	SiO_2	TiO_2	Al_2O_3	MgO	CaO	MnO	FeO*	Na_2O	K_2O	Sum	An	Ab	Or	$Kd^{Ca\text{-}Na}$
T15	2	51.70	0.03	29.58	0.18	13.84	0.00	0.66	3.42	0.16	99.56	68.48	30.58	0.94	1.76
sd		0.28	0.04	0.13	0.04	0.14	0.00	0.03	0.05	0.02	0.28	0.01	0.11	0.13	
T16	1	54.13	0.16	26.58	0.33	10.69	0.00	0.97	4.64	0.40	97.88	54.65	42.93	2.42	1.15
T24	1	52.01	0.02	29.10	0.23	12.96	0.10	0.75	3.91	0.14	99.20	64.18	35.02	0.81	1.56
T31	2	53.66	0.13	26.37	0.39	10.79	0.01	0.98	4.63	0.42	97.39	54.90	42.56	2.54	1.40
sd		1.55	0.04	1.13	0.31	0.05	0.01	0.19	0.22	0.02	2.49	1.07	1.04	0.03	
T32	1	55.27	0.13	26.90	0.10	9.97	0.00	0.54	5.33	0.40	98.64	49.64	47.97	2.38	1.16
T35	1	56.31	0.09	26.75	0.11	9.63	0.11	0.65	5.52	0.46	99.63	47.73	49.55	2.72	0.94
T36	1	56.59	0.10	26.60	0.15	9.62	0.03	1.01	5.29	0.51	99.90	48.62	48.33	3.05	1.23
T53	1	55.58	0.17	26.82	0.11	10.49	0.06	0.56	5.24	0.41	99.44	51.28	46.33	2.40	1.36
T39	1	56.67	0.00	26.95	0.39	11.15	0.00	0.97	3.72	0.16	100.02	61.70	37.25	1.05	1.95
T43	1	57.52	0.00	26.53	0.17	9.64	0.00	0.90	5.08	0.55	100.39	49.48	47.14	3.37	1.31
T7		55.66	0.00	27.25	0.47	11.86	0.00	0.55	4.18	0.22	100.18	60.28	38.42	1.31	1.56
T8	2	56.89	0.08	26.44	0.39	10.81	0.11	0.63	4.36	0.33	100.02	56.62	41.33	2.05	1.76
sd		1.31	0.11	0.94	0.33	0.55	0.15	0.10	0.23	0.11	0.03	0.37	0.19	0.56	

T46	1	53.79	0.07	27.95	0.09	11.94	0.10	0.64	4.59	0.18	99.36	58.34	40.59	1.07	1.57
T47	1	58.47	0.05	24.03	0.36	8.32	0.00	0.97	4.69	0.91	97.80	46.48	47.46	6.06	1.29
T48	1	58.10	0.18	24.84	0.16	8.21	0.04	1.00	5.72	0.91	99.15	41.81	52.66	5.53	
T54	1	53.51	0.06	27.09	0.49	12.64	0.14	1.06	3.27	0.32	98.57	66.76	31.23	2.01	2.08
T55	1	54.87	0.15	26.26	0.34	11.23	0.07	1.11	4.27	0.45	98.76	57.63	39.59	2.77	1.87
T56	1	56.17	0.15	25.03	0.55	10.27	0.02	1.13	4.87	0.52	98.71	52.14	44.72	3.14	1.43

An= 100[Ca/(Ca+Na+K)]; Ab= 100[Na/(Ca+Na+K)]; Or=[100K/(Ca+Na+K)]. End-members calculated as in Deer *et al*. (1972).

$Kd^{Ca\text{-}Na}$= (Ca/Na in plagioclase)/(Ca/Na in melt)

Table 7: Representative compositions of experimental Fe-Ti oxides

	n	SiO_2	TiO_2	Al_2O_3	MgO	CaO	MnO	FeO*	Na_2O	K_2O	Cr_2O_3	Sum	Mg#
T19	1	0.18	11.80	4.12	3.65	0.22	0.29	68.75	0.00	0.09	-	89.09	5.04
T20	1	3.51	13.78	4.33	3.59	0.37	0.29	67.50	0.46	0.20	-	94.01	5.05
T21	1	0.19	15.94	3.35	3.49	0.15	0.17	68.46	0.00	0.05	-	91.80	4.85
T22	1	2.27	43.94	0.46	5.22	0.42	0.41	43.41	0.00	0.09	-	96.23	
T23	1	0.24	5.30	5.02	4.67	0.22	0.37	76.47	0.01	0.02		92.31	5.75
T24	1	0.33	7.22	5.5	4.65	0.46	0.21	75.03	0.05	0.88	0.64	100.64	5.4
T25	1	1.44	8.77	4.46	4.01	0.29	0.37	74.15	0.21	0.09		93.78	5.13
T4	1	4.01	43.79	1.36	3.81	0.40	0.26	41.13	0.46	0.18		95.41	
T47b	2	1.29	9.21	5.89	4.50	0.37	0.36	65.52	0.10	0.02	5.35	92.62	6.42
sd		0.83	0.08	0.24	0.31	0.17	0.02	0.81	0.04	0.02	0.04	0.66	
T53	2	3.15	11.85	7.05	3.90	0.38	0.33	54.25	0.30	0.21	11.89	93.31	6.71
sd		0.14	0.47	0.86	0.21	0.01	0.00	0.50	0.10	0.11	0.02	0.24	
T38	1	1.67	5.48	6.53	4.23	0.26	0.14	68.46	0.09	0.09	3.62	90.56	5.82
T40	1	1.30	11.81	4.67	3.00	0.32	0.24	68.22	0.07	0.04	1.26	90.95	4.21
T39	1	0.35	8.26	5.42	3.52	0.26	0.33	68.45	0.00	0.01	1.12	87.70	4.89
T41	1	0.15	5.21	4.23	3.35	0.18	0.21	76.61	0.04	0.04	1.20	91.22	4.18
T42	2	0.13	5.71	4.89	2.73	0.23	0.25	74.61	0.00	0.03	1.32	89.90	3.53

sd		0.02	0.20	0.06	0.01	0.11	0.03	1.21	0.00	0.03	0.11	1.44	
T43	1	0.14	8.29	4.51	2.61	0.21	0.25	73.81	0.00	0.11	0.79	90.71	3.41
T44	1	0.16	10.85	3.47	2.59	0.22	0.14	72.21	0.02	0.00	1.41	91.05	3.46
T45	1	0.16	3.60	3.88	3.10	0.09	0.46	76.15	0.05	0.05	2.47	90.01	3.91
T46	1	0.51	4.08	4.73	2.97	0.13	0.48	87.13	0.00	0.05	-	100.00	3.30
T8	1	0.38	15.05	3.49	2.97	0.29	0.35	70.76	0.02	0.05	1.52	94.88	4.02
T8	1	1.07	44.20	0.80	3.83	0.50	0.38	44.50	0.15	0.04	0.22	95.67	7.92
T7	1	0.88	14.13	4.28	3.27	0.28	0.00	71.03	0.05	0.15	1.03	94.07	4.40
T46	1	0.16	4.25	3.92	2.81	0.12	0.15	80.01	0.03	0.08	1.50	91.54	3.39
T47	1	0.31	4.80	3.60	2.46	0.21	0.30	77.91	0.00	0.00	1.86	89.59	3.06
T48	1	0.42	7.53	3.16	2.27	0.23	0.19	77.91	0.04	0.08	1.23	91.84	2.83
T54	2	0.25	7.60	5.20	5.00	0.18	0.30	79.13	0.02	0.05	2.25	100.00	5.94
sd		0.02	0.13	0.24	0.10	0.03	0.05	0.15	0.00	0.03	0.09	0.00	
T55	2	0.15	9.92	4.50	4.39	0.16	0.22	79.25	0.01	0.00	1.40	100.00	5.25
sd		0.09	0.01	0.09	0.09	0.12	0.05	0.40	0.01	0.00	0.55	0.00	
T56	2	0.17	10.32	4.07	4.27	0.10	0.36	78.10	0.00	0.03	2.58	100.00	5.18
sd		0.08	0.49	0.13	0.09	0.07	0.04	0.64	0.00	0.03	1.22	0.00	

n: number of analyses   sd: standard deviation

Mg#=100*(MgO/MgO+FeO*)

Table 8: Composition of experimental amphiboles

sample	T6	sd	T7	T38	sd	T41	sd	T42	sd	T43	T45	sd	T46	T47
n	3		1	3		3		2		1	3		1	2
SiO_2	43.23	0.80	41.74	42.99	0.40	43.41	0.19	42.29	0.27	42.60	42.98	0.54	42.35	44.01
TiO_2	2.39	0.13	3.91	2.26	0.05	1.96	0.29	2.30	0.09	2.87	1.82	0.16	2.31	2.23
Al_2O_3	11.23	0.17	11.53	11.80	0.31	11.74	0.22	12.19	0.02	11.66	11.93	0.18	12.28	10.64
MgO	14.69	0.08	13.13	15.28	0.11	15.22	0.43	14.18	0.14	14.22	14.88	0.35	14.20	14.90
CaO	11.16	0.28	10.98	11.40	0.18	11.53	0.34	11.36	0.08	11.38	11.83	0.15	11.93	10.89
MnO	0.11	0.07	0.08	0.10	0.12	0.17	0.10	0.13	0.05	0.07	0.20	0.04	0.05	0.26
FeO*	10.63	0.73	11.56	9.84	0.37	10.48	0.65	11.96	0.30	11.97	10.71	0.59	11.08	11.26
Na_2O	2.17	0.13	2.25	2.21	0.08	2.10	0.03	2.18	0.09	2.21	2.05	0.04	2.14	2.00
K_2O	0.48	0.07	0.57	0.57	0.07	0.56	0.06	0.56	0.04	0.67	0.60	0.03	0.76	0.56
Sum	96.09	1.33	95.75	96.46	0.32	97.18	0.62	97.15	0.11	97.65	97.00	0.81	97.09	96.75
Si	6.31		6.19	6.23		6.25		6.13		6.17	6.23		6.18	6.35
Ti	0.26		0.44	0.25		0.21		0.25		0.31	0.20		0.25	0.24
Al	1.93		2.02	2.02		1.99		2.08		1.99	2.04		2.11	1.81
Fe+3	0.74		0.47	0.76		0.84		0.90		0.77	0.75		0.53	0.97
Fe+2	0.55		0.96	0.43		0.42		0.55		0.68	0.55		0.82	0.39
Mn	0.01		0.01	0.01		0.02		0.02		0.01	0.02		0.01	0.03

Mg	3.19		2.91	3.30		3.27		3.07		3.07	3.21		3.09	3.21
Ca	1.74		1.75	1.77		1.78		1.76		1.77	1.84		1.87	1.68
Na	0.61		0.65	0.62		0.59		0.61		0.62	0.58		0.61	0.56
K	0.09		0.11	0.11		0.10		0.10		0.12	0.11		0.14	0.10
H	2.00		2.00	2.00		2.00		2.00		2.00	2.00		2.00	2.00
P *(MPa):	386.32		396.32	444.29		439.93		481.37		406.34	437.39		419.22	386.77
T*(ºC):	867.34		865.36	885.78		886.26		900.18		882.06	866.52		826.32	910.84
ΔNNO*:	3.03		0.76	3.95		4.13		3.42		2.75	4.08		3.25	3.74
H_2O_{melt}*:	4.43		3.86	4.58		4.71		4.58		4.18	5.33		5.90	3.61

n: number of analysis

sd: standard deviation

*pamameters calculated using the Ridolfi &Renzulli (2012) equations

Table 9: Average composition of experimental glasses

NNO+1 experiments

	n												
1000ºC/100MPa		SiO_2	TiO_2	Al_2O_3	FeO*	MnO	MgO	CaO	Na_2O	K_2O	P_2O_5	Total	Sum
T15	11	59.97	0.87	17.37	6.27	0.13	2.89	6.30	4.03	1.90	0.27	100.00	94.55
sd		0.27	0.09	0.24	0.28	0.08	0.10	0.13	0.10	0.12	0.06	0.00	0.74
T16	1	61.36	0.96	16.51	6.26	0.12	2.46	5.62	4.11	2.25	0.34	100.00	93.66
T18	4	63.72	1.33	16.47	4.93	0.09	1.61	4.30	4.25	2.86	0.45	100.00	96.01
sd		0.59	0.15	0.80	0.38	0.05	0.09	0.53	0.12	0.28	0.10	0.00	0.66
975ºC/100MPa													
T19	4	61.99	0.93	17.35	5.65	0.07	2.02	5.26	4.21	2.18	0.36	100.00	92.92
sd		0.22	0.12	0.27	0.24	0.09	0.07	0.22	0.11	0.07	0.14	0.00	0.55
T20	7	63.91	0.95	16.28	5.22	0.09	1.63	4.22	4.50	2.78	0.40	100.00	93.04
sd		0.45	0.10	0.43	0.18	0.11	0.07	0.21	0.06	0.08	0.11	0.00	0.57
1000ºC/200MPa													
T10	15	60.19	0.88	16.84	6.08	0.14	3.42	6.71	3.89	1.71	0.13	100.00	92.45
sd		0.44	0.06	0.17	0.22	0.09	0.08	0.11	0.16	0.12	0.09	0.00	0.43
T11	15	60.10	0.94	17.66	5.94	0.13	2.91	6.25	4.10	1.82	0.16	100.00	94.64
sd		0.47	0.08	0.61	0.28	0.10	0.33	0.39	0.15	0.13	0.09	0.00	0.60

T12	7	61.54	1.08	16.81	5.95	0.03	2.42	5.57	4.28	2.15	0.17	100.00	94.24
sd		0.43	0.03	0.16	0.21	0.02	0.05	0.30	0.08	0.09	0.09	0.00	0.19
975ºC/200MPa													
T1	6	60.06	0.88	17.93	6.15	0.08	2.53	6.13	4.06	1.85	0.31	100.00	93.06
sd		0.29	0.08	0.27	0.24	0.08	0.04	0.10	0.11	0.06	0.10	0.00	0.36
T2	6	62.12	1.03	16.97	5.93	0.03	2.06	5.24	4.20	2.22	0.21	100.00	93.59
sd		0.25	0.10	0.11	0.23	0.05	0.02	0.12	0.07	0.09	0.08	0.00	0.69
T3	2	62.50	1.04	16.86	5.87	0.11	1.65	4.88	4.37	2.37	0.36	100.00	93.78
sd		0.12	0.08	0.21	0.08	0.14	0.00	0.24	0.35	0.10	0.02	0.00	0.39
T4	5	64.83	0.90	16.05	4.91	0.10	1.25	3.66	4.61	3.27	0.42	100.00	94.44
sd		0.18	0.06	0.08	0.18	0.10	0.04	0.05	0.11	0.06	0.11	0.00	0.22
950ºC/200MPa													
T6	10	61.56	0.68	17.70	5.87	0.11	2.36	5.75	3.80	1.94	0.23	100.00	92.38
sd		0.26	0.09	0.08	0.27	0.07	0.07	0.13	0.10	0.11	0.13	0.00	0.52
T7	1	62.62	0.83	17.17	5.91	0.18	1.84	4.55	4.08	2.61	0.21	100.00	93.65
T8	3	64.56	0.89	16.48	5.14	0.01	1.30	3.91	4.39	3.10	0.23	100.00	94.46
sd		0.21	0.10	0.36	0.13	0.01	0.05	0.14	0.06	0.12	0.06	0.00	0.08
1025ºC/400 MPa													
T28	12	59.27	0.88	16.89	6.22	0.09	4.13	6.98	3.58	1.74	0.23	100.00	12.31
sd		0.28	0.11	0.20	0.22	0.08	0.21	0.24	0.11	0.23	0.11	0.00	0.60

T29	6	59.10	0.86	17.51	6.29	0.12	3.62	6.53	3.98	1.77	0.21	100.00	8.12
sd		0.47	0.05	0.38	0.34	0.05	0.36	0.40	0.15	0.04	0.12	0.00	0.26
T30	8	59.21	0.89	17.87	6.08	0.04	3.29	6.36	4.27	1.79	0.20	100.00	7.49
sd		0.37	0.11	0.11	0.25	0.06	0.03	0.15	0.07	0.06	0.11	0.00	0.37
T31	1	63.04	1.28	15.83	6.39	0.01	1.82	4.58	4.28	2.66	0.10	100.00	5.83
T32	4	63.11	1.16	16.11	5.78	0.17	1.73	4.35	4.33	2.96	0.31	100.00	95.10
sd		0.19	0.08	0.13	0.16	0.12	0.04	0.14	0.04	0.07	0.05	0.00	0.45

1000ºC/400MPa

T33	10	60.03	0.91	17.35	6.14	0.07	3.40	6.43	3.57	1.80	0.30	100.00	9.88
sd		0.31	0.10	0.16	0.28	0.06	0.07	0.12	0.16	0.10	0.11	0.00	0.61
T34	2	59.96	0.93	17.93	6.23	0.05	2.91	5.93	3.91	1.85	0.30	100.00	6.93
sd		0.39	0.06	0.34	0.44	0.09	0.13	0.03	0.10	0.02	0.02	0.00	0.00
T35	2	61.60	1.05	17.94	5.46	0.05	1.87	5.15	4.24	2.31	0.33	100.00	5.53
sd		0.32	0.02	0.37	0.14	0.07	0.08	0.34	0.17	0.42	0.26	0.00	0.18
T36	3	63.69	1.12	16.93	5.92	0.09	1.56	4.45	4.54	2.61	0.33	100.00	4.89
sd		0.50	0.11	0.16	0.20	0.05	0.07	0.16	0.08	0.16	0.12	0.00	0.80

NNO+2 experiments

1000ºC/100MPa

T54	4	61.95	0.99	16.92	5.33	0.20	2.51	5.61	4.22	2.01	0.25	100.00	94.69

sd		0.84	0.04	0.36	0.09	0.14	0.04	0.23	0.11	0.05	0.05	0.00	0.45
T55	7	63.88	0.98	16.24	4.85	0.10	2.05	4.51	4.68	2.55	0.17	100.00	95.08
sd		0.32	0.14	0.21	0.38	0.09	0.03	0.12	0.11	0.17	0.07	0.00	0.50
T56	5	64.93	1.02	15.73	4.67	0.14	1.77	4.24	4.46	2.74	0.30	100.00	95.64
sd		0.34	0.11	0.28	0.14	0.10	0.05	0.13	0.08	0.08	0.12	0.00	0.70
T57	2	67.10	0.96	14.95	4.30	0.08	1.41	3.21	4.34	3.50	0.14	100.00	96.90
sd		0.56	0.10	0.14	0.07	0.04	0.22	0.07	0.06	0.12	0.06	0.00	0.58
1000ºC/200MPa													
T45b	2	60.07	0.93	17.24	6.17	0.13	3.36	6.53	3.58	1.73	0.25	100.00	92.48
sd		0.23	0.15	0.03	0.25	0.06	0.07	0.00	0.01	0.11	0.08	0.00	0.02
T46b	3	60.45	0.85	17.86	5.79	0.14	2.98	6.11	3.78	1.94	0.11	100.00	93.36
sd		0.52	0.07	0.21	0.45	0.07	0.09	0.01	0.03	0.02	0.09	0.00	0.53
T47b	5	61.71	0.97	16.77	6.02	0.13	2.38	5.30	4.18	2.31	0.22	100.00	93.94
sd		0.34	0.04	0.20	0.34	0.07	0.05	0.13	0.12	0.10	0.07	0.00	0.80
975ºC/200MPa													
T23	11	60.64	0.83	17.81	5.43	0.09	2.99	6.08	4.05	1.86	0.22	100.00	92.12
sd		0.29	0.09	0.18	0.29	0.08	0.06	0.10	0.14	0.07	0.07	0.00	0.62
T24	6	61.09	0.80	17.86	5.63	0.12	2.64	5.53	4.05	2.01	0.26	100.00	93.40
sd		0.21	0.11	0.15	0.22	0.08	0.06	0.04	0.11	0.12	0.16	0.00	0.62

T25	1	63.22	0.84	16.52	4.96	0.00	2.35	4.45	4.45	2.57	0.39	100.00	2.11
1025/400MPa													
T49	4	59.33	0.92	16.55	5.91	0.20	4.08	6.99	4.07	1.79	0.16	100.00	89.60
sd		0.43	0.10	0.17	0.38	0.11	0.06	0.12	0.25	0.17	0.13	0.00	
T50	10	59.45	0.82	17.02	6.21	0.17	3.58	6.49	4.17	1.79	0.30	100.00	93.01
sd		0.38	0.08	0.21	0.35	0.12	0.09	0.10	0.09	0.08	0.10	0.00	
T51	8	59.58	0.90	17.81	5.99	0.13	2.83	6.15	4.46	1.91	0.24	100.00	94.88
sd		0.40	0.10	0.25	0.32	0.09	0.15	0.15	0.10	0.07	0.13	0.00	
T52	2	61.12	1.13	17.15	5.67	0.13	2.27	5.36	4.69	2.10	0.38	100.00	95.43
sd		0.14	0.03	0.30	0.36	0.13	0.02	0.00	0.08	0.08	0.13	0.00	
T53	4	62.82	1.32	15.92	5.73	0.07	1.82	4.42	4.67	2.84	0.40	100.00	95.87
sd		0.24	0.06	0.25	0.12	0.05	0.03	0.09	0.05	0.10	0.10	0.00	
1000ºC/400 MPa													
T37	10	59.70	0.86	17.20	6.10	0.12	3.67	6.28	4.02	1.82	0.22	100.00	90.28
sd		0.43	0.12	0.17	0.34	0.10	0.07	0.18	0.14	0.13	0.08	0.00	
T38	10	60.83	0.79	17.64	5.57	0.13	2.93	5.89	3.96	1.98	0.30	100.00	92.20
sd		0.26	0.09	0.18	0.20	0.09	0.08	0.17	0.41	0.08	0.07	0.00	
T39	1	62.41	0.96	17.65	4.78	0.08	2.00	4.98	4.45	2.41	0.27	100.00	93.50
975ºC/400MPa													
T41	3	62.94	0.62	17.78	4.89	0.04	2.01	5.92	3.51	1.94	0.33	100.00	89.91

sd		0.21	0.05	0.07	0.38	0.05	0.10	0.01	0.15	0.12	0.12	0.00	
T43	3	65.27	0.59	16.48	4.06	0.06	1.79	4.27	4.47	2.65	0.36	100.00	93.85
sd		0.39	0.10	0.20	0.14	0.09	0.14	0.16	0.24	0.11	0.11	0.00	
950ºC/400 MPa													
T45	4	64.13	0.47	17.66	4.12	0.18	1.60	5.57	3.99	2.02	0.26	100.00	90.72
sd		0.28	0.12	0.20	0.28	0.04	0.05	0.05	0.15	0.06	0.06	0.00	
T46	2	66.45	0.39	16.66	3.69	0.17	1.31	4.47	4.39	2.30	0.15	100.00	92.60
sd		0.10	0.08	0.02	0.28	0.04	0.00	0.06	0.23	0.03	0.12	0.00	
T47	1	70.20	0.37	15.89	2.93	0.03	0.86	2.95	3.72	3.06	0.00	100.00	94.47

Legend as in previous Tables.